UCLA
UCLA Electronic Theses and Dissertations

Title
High pressure and temperature equations of state: A tool for insight into deep Earth systems

Permalink
https://escholarship.org/uc/item/387964f3

Author
Armentrout, Matthew Martin

Publication Date
2012

Peer reviewed|Thesis/dissertation

eScholarship.org Powered by the California Digital Library
University of California

UNIVERSITY OF CALIFORNIA

Los Angeles

High pressure and temperature equations of state:

A tool for insight into deep Earth systems

A dissertation submitted in partial satisfaction of

the requirements for the degree Doctor of Philosophy

in Geochemistry

By

Matthew Martin Armentrout

2012

© Copyright by

Matthew Martin Armentrout

2012

ABSTRACT OF THE DISSERTATION

High pressure and temperature equations of state:

A tool for insight into deep Earth systems

By

Matthew Martin Armentrout

Doctor of Philosophy in Geochemistry

University of California, Los Angeles, 2012

Professor Abby Kavner, Chair

High pressure and temperature equations of state are powerful tools for probing the behavior of matter at extreme conditions. The recent deployment of third generation synchrotron light sources combined with stable, reproducible laser heating has allowed the measurement of high pressure and temperature equations of state in the diamond anvil cell. In this document I leverage this new capability to address several types of questions in the Earth sciences. Measurements of osmium metal are used to investigate different formulations of the equation of state and the measurement of very incompressible materials. Measurements of iron ringwoodite are used to examine trade-offs in seismic observables with thermal and compositional anomalies. Finally, the equation of state of cobalt oxide is used to make predictions about redox relations in the early Earth during core formation.

The dissertation of Matthew Martin Armentrout is approved.

Paul Davis

Craig Manning

Sarah Tolbert

Abby Kavner, Committee Chair

University of California, Los Angeles

2012

Table of Contents

List of Figures and Tables

Acknowledgements

The first chapter of this thesis is a version of a Journal of Applied Physics article (Armentrout, M. M. and A. Kavner (2010), Incompressibility of osmium metal at ultrahigh pressures and temperatures, *J. App. Phys.*, **107**, 093528). The second chapter of this thesis is a evrsion of an article published in Geophysical Research Letters (Armentrout, M. M. and A. Kavner (2011), High pressure, high temperature equation of state for Fe2SiO4 ringwoodite and implications for the Earth's transition zone, *Geophys. Res. Lett.*, **38**, L08309). For each of these I owe a debt of gratitude to my advisor and co-author Professor Abby Kavner.

Portions of this work were performed at GeoSoilEnviroCARS (Sector 13) and HPCAT (sector 16), Advanced Photon Source (APS), Argonne National Laboratory. GeoSoilEnviroCARS is supported by the National Science Foundation - Earth Sciences (EAR-1128799) and Department of Energy - Geosciences (DE-FG02-94ER14466). HPCAT is supported by CIW, CDAC, UNLV and LLNL through funding from DOE-NNSA, DOE-BES and NSF. Use of the Advanced Photon Source was supported by the U. S. Department of Energy, Office of Science, Office of Basic Energy Sciences, under Contract No. DE-AC02-06CH11357.

Other portions of this work were performed at end-station 12.2.2 at the Advanced Light Source. The Advanced Light Source is supported by the Director, Office of Science, Office of Basic Energy Sciences, of the U.S. Department of Energy under Contract No. DE-AC02-05CH11231.

Vitae

Matthew Martin Armentrout
University of California, Los Angeles
595 Charles Young Drive East
3806 Geology Building
Los Angeles, CA 90095
E-mail: armentrout@ucla.edu

Education

B.S. Geology, California Institute of Technology, 2006
M.S. Geochemistry, University of California, Los Angeles, 2009
Ph.D. Geochemistry (expected completion June 2012), University of California Los Angeles

Publications

Xie, M., R. Mohammadi, Z. Mao, **M. M. Armentrout**, A. Kavner, R. B. Kaner, and S. H. Tolbert, (2012), Exploring the High Pressure Behavior of Superhard Tungsten Tetraboride, *Phys. Rev. B*, (in press)

Z., Mao, **M. M. Armentrout**, E. Rainey, et al., (2011), Dolomite III: A new candidate lower mantle carbonate, *Geophys. Res. Lett.*, 38, L22303

Kavner, A., **M. M. Armentrout**, E. S. G. Rainey, M. Xie, B. E. Weaver, S. H. Tolbert, and R. B. Kaner, (2011), Thermoelastic properties of ReB2 at high pressures and temperatures and comparison with Pt, Os, and Re, *J. Appl. Phys.*, 110, 093518-093515

Armentrout, M. M. and A. Kavner, (2011), High pressure, high temperature equation of state for Fe2SiO4 ringwoodite and implications for Earth's transition zone, *Geophys. Res. Lett.*, 38, L08309

Armentrout, M. M. and A. Kavner, (2010), Incompressibility of osmium metal at ultrahigh pressures and temperatures, *J. App. Phys.*, 107, 093528

Armentrout, M. M., F.-X. Li,, and P. B. Armentrout, (2004), Is Spin Conserved in Heavy Metal Systems? Experimental and Theoretical Studies of the Reaction of Re+ with Methane, *J. Phys. Chem.*, 108, 9660-9672

Introduction

Equations of state are useful tools for probing the behavior of the vast majority of the matter composing the Earth. They relate the extensive thermodynamic property volume with the intensive properties temperature and pressure. This allows the calculation of density at conditions of the deep Earth, interpretation of seismic observables, and the prediction of high pressure phenomena. In this sense, high pressure experiments form a bridge, linking together the fields of seismology, geodynamics, and petrology.

The deployment of third generation synchrotron light sources in conjunction with diamond anvil cells permitted measurements of isothermal equations of state up to pressures of the Earth's core. The further development of stable, reproducible *in situ* laser heating has expanded the capability of these facilities to the measurement of simultaneous high pressure and temperature equations of state. In this document I address several scientific questions using high pressure and temperature equations of state measured in the laser heated diamond anvil cell using synchrotron X-ray diffraction.

Osmium is a third row transition metal and one of the most incompressible elements. It is of interest as an extremely incompressible metal and as a possible analog for iron at high pressure. We use the equation of state of osmium as a test-bed for different formulations of the equation of state and as a test of the efficacy of using multiple pressure standards during multiple experiments at multiple synchrotron beamlines. The compressibility and thermal expansion of osmium is compared to other transition metal oxides.

Ringwoodite is a spinel-structured silicate and is the dominant mineral in the lower transition zone. We measured the equation of state of iron end-member ringwoodite at conditions of the transition zone. This is used to make predictions on the sensitivity of density and bulk

sound velocity to thermal and compositional variation. The results show that variations in iron content and temperature have opposing effects on density and bulk sound velocity, suggesting that lateral variations in composition (iron content) and temperature in the transition zone may be distinguished using seismic observables.

The high-pressure high-temperature equation of state of cobalt oxide was measured at conditions of the lower mantle. Cobalt oxide was observed to be stable in the B1 rocksalt phase throughout this pressure and temperature range. This newly determined equation of state is used in conjunction with existing thermoelastic parameters for cobalt metal a to calculate the redox energetics of the CoO/Co system as a function of pressure and temperature. A comparison with related transition metal oxide systems predicts an exchange reaction between NiO and CoO at pressures of ~30 GPa, qualitatively similar to independent observations of a crossover in the partitioning behaviors of nickel and cobalt between silicate and metal at similar conditions.

Incompressibility of osmium metal at ultrahigh pressures and temperatures

Abstract

Osmium is one of the most incompressible elemental metals, and is used as a matrix material for synthesis of ultra-hard materials. To examine the behavior of osmium metal under extreme conditions of high pressure and temperature, we measured the thermal equation of state of osmium metal at pressures up to 50 GPa and temperatures up to 3000 K. X-ray diffraction measurements were conducted in the laser heated diamond anvil cell at GSECARS and HPCAT at the Advanced Photon Source and beamline 12.2.2 at the Advanced Light Source. Ambient temperature data give a zero pressure bulk modulus of 421 (3) GPa with a first pressure derivative fixed at 4. Fitting to a high temperature Birch-Murnaghan equation of state gives a room pressure thermal expansion of 1.51 (0.06)E-5 K^{-1} with a first temperature derivative of 4.9 (0.7)E-9 K^{-2} and the first temperature derivative of bulk modulus of be dK_0/dT = -0.055 (0.004). Fitting to a Mie-Grüneisen-Debye equation of state gives a Grüneisen parameter of 2.32 (0.08) with a q of 7.2 (1.4). A comparison of the high pressure, temperature behavior among Re, Pt, Os, shows that Os has the highest bulk modulus and lowest thermal expansion of the three, suggesting that Os-based ultra-hard materials may be especially mechanically stable under extreme conditions.

1. Introduction

Osmium, a third row transition metal in the iron group, has a hexagonal close-packed structure and is characterized by its high density, extremely low compressibility (Cynn et al. 2002; Kenichi 2004; Occelli et al. 2004; Voronin et al. 2005; Weinberger et al. 2008; Pantea et al. 2009) and high hardness (Shackleford 2001). These properties make osmium a potentially important matrix material for the synthesis of ultra-hard materials. For example, addition of boron (Cumberland et al. 2005; Hebbache et al. 2006) raises osmium's Vicker's hardness from 400 kg/mm^2 to 2000-3000 kg/mm^2 while reducing the bulk modulus from 421 to 365 GPa (Cumberland et al. 2005). Carbon and nitrogen (Zheng 2005) are also thought to have a similar effect. We are interested in characterizing the density and thermoelastic equation of state for osmium at extreme conditions of high pressure and temperature to establish the baseline behavior of pure osmium metal as a launching point for characterizing the high P,T behavior of ultra-hard materials based on third-row transition metals.

While osmium's high pressure and room temperature P(V) equation of state and strength have been extensively studied (Cynn et al. 2002; Kenichi 2004; Occelli et al. 2004; Voronin et al. 2005; Weinberger et al. 2008; Pantea et al. 2009), there is only a single study of the of the high pressure high-temperature thermoelastic properties of Os (Voronin et al. 2005). Voronin et al. (2005) used *in-situ* X-ray diffraction with a mulitanvil device to measure the density of osmium up to 15 GPa and 1273 K (Table 1). Our objective is to overlap and extend this study to pressures of 50 GPa and temperatures up to ~3000 K. The ultimate goal is to measure the thermoelastic equation of state for pure osmium metal to be used as a baseline for comparison with the thermal behavior of third-row transition metal-based ultra-hard materials.

2. Experimental procedure

High pressure, high temperature X-ray diffraction experiments using the laser-heated diamond anvil cell were performed on Os metal at three different beamlines: 12.2.2 at the Advanced Light Source (ALS), 13-ID-D at GSECARS and 16-ID-D HPCAT, both at the Advanced Photon Source (APS). This redundancy allows this study to function as a check on the agreement between data collected at multiple beamlines and with different pressure standards.

The starting sample consisted of 99.8% pure osmium metal powder ~1μm (Alfa Aesar). Foils were prepared by compressing Os powder between diamonds to a thickness of ~10 μm, and loaded into diamond cells equipped with pre-indented, drilled rhenium gaskets, and either 300 μm or 500 μm culet diamonds. Experiments performed at the ALS had the osmium sample loaded between plates of NaCl, which functioned as both a pressure standard and a thermal insulator. At the APS osmium samples were loaded on top of 10 μm plates of MgO powder that served as primary pressure standards and as spacers between sample and diamond. Ruby spherules were loaded on the periphery to serve as a secondary pressure standard. The sample chamber was loaded with neon gas at 25 kbar using the gas loading system at GSECARS (Rivers et al. 2008).

Each experiment consisted of a series of angle-dispersive monochromatic X-ray diffraction measurements made before heating, during laser heating, and after quench, with ~30 sec. exposure times. A summary of experimental conditions at different beamlines, X-ray wavelength, X-ray beam size, pressure range, temperature range, and pressure standard is tabulated in Table 2.

Heating of the Os sample was achieved using double-sided laser heating with fiber lasers. Each beamline has broadly similar setups for laser heating and temperature measurements. Optical setups at ALS 12.2.2, HPCAT, and GSECARS are described in more depth in (Caldwell et al. 2007; Meng et al. 2006; Prakapenka et al. 2008) respectively. Temperatures were obtained using in-house temperature measurement software from each facility (Caldwell et al. 2007; Meng et al. 2006; Prakapenka et al. 2008).

Emitted Planck radiation from the sample hotspot was collected and fit to a Planck curve between 590 and 740 nm at the ALS and 600-800 at HPCAT and GSECARS. Temperatures were measured one to three times on each side of the sample during each diffraction measurement. Temperature variation over time was routinely smaller (~1%) than the variation between each side of the sample (~8%). The measured surface temperature was taken to be the mean value of these measurements. The error on the measured temperature was calculated using the deviation of individual measurements from the mean.

Radial heated spot sizes were typically much larger than the X-ray spots (Table 2), which minimizes radial temperature errors (Kavner and Panero 2004). Modeling of axial temperature gradients (Campbell et al. 2007) of double-sided laser-heated samples of optically opaque iron sulfate in an insulating medium found a 10% drop in the center temperature. This correlates to a drop in average temperature of 7% over the X-ray volume compared to the average surface temperature. Therefore we apply a -7% correction to the measured sample temperatures in this study.

Angle-dispersive X-ray diffraction patterns were collected using each of the beamline's imaging plate systems. Sample to detector distances were calibrated using a LaB_6 standard at the ALS and CeO_2 standards at HPCAT and GSECARS. Intensity vs. two-theta X-ray diffraction

patterns were generated from the two-dimensional image using the software Fit2D (Hammersley et al. 1996). Diffraction patterns were then indexed, and individual *d*-spacings determined by a Gaussian fit to each diffraction peak as in Figure 1. In the case of overlapping diffraction lines we used double Gaussian fits to more accurately resolve each peak. The a and c lattice parameters of osmium were calculated from the *d*-spacings of diffraction peaks (100), (002), (101), and (102) using a least-squares linear fit to the hexagonal lattice. Lattice parameters of B1 NaCl were determined using the (111), (200), (220), and (222) diffraction lines. At pressures above the NaCl phase transformation (~25-30 GPa) NaCl B2 lattice parameters were determined using the (100) and (110) diffraction lines. MgO lattice parameters were determined using the (200), (220), (311), and (222) diffraction lines. Lattice parameters of sample and standards, and temperature and pressure data are summarized in Table A1 in Appendix A.

We assume sample and pressure standard to be isobaric in this study. Pressures of standard materials were determined by fitting the measured lattice parameters of NaCl B1 or B2 or MgO to their high pressure, high temperature equations of state using an isothermal third order Birch-Murnaghan equation of state in conjunction with a Mie-Grüneisen-Debye model of thermal pressure. The formalisms of these models are more fully explained in the results section and in references (Jackson and Rigden 1996; Duffy and Wang 1998; Dorogokupets and Dewaele 2007). Equation of state parameters for both NaCl and MgO were taken from Dorogokupets and Dewaele (2007). Since the pressure standards also acted as insulation layers between the sample and the diamonds, their temperatures were assumed to be halfway between the measured temperatures and 300 K (Campbell et al. 2007; Dewaele et al. 1998; Kiefer and Duffy 2005). Pressure errors are a result of uncertainties on the lattice parameters of the pressure calibrants, uncertainty on the equation of state parameters, uncertainties in calibrant temperature and the

effects of possible nonhydrostatic stresses on lattice parameter measurement. In the diamond anvil cell, any nonhydrostatic stresses tend to yield an overestimate of the lattice *d*-spacing measured in the normal X-ray direction. If three dimensional stresses are present but not considered, lattice volume will be overestimated and therefore pressure will be underestimated (Weinberger et al. 2008; Meng and Weidner 1993).

3. Results

Volume-temperature paths for Os during two characteristic heating cycles are shown in Figure 2. During heating, the osmium lattice parameters follow complicated paths, neither constant volume nor constant pressure, similar to observations by Kavner and Duffy (2001). In general, the heating path follows a different trajectory than the cooling path, and the paths are not necessarily bound within constant volume and constant pressure behavior. The sample and standard paths generally show better correlation at high temperature than at room temperature. These results suggest that lack of hydrostaticity may be compromising the pressure measurements especially at room temperature. In general, the preheat volumes are lower than the quench volumes (although this is not always the case). The error bars on the Os volume vary widely—both within a heating cycle and between heating cycles (e.g. both larger (1.57%) and smaller (0.06%) volume error bars are present in Figures 2a and 2c), While the Gaussian fits to each peak are precise to ~0.001%, these volume uncertainties arise from the fit to the hexagonal close-packed Os lattice-- an additional possible indicator of nonhydrostaticity in these measurements.

Given the large degree of uncertainty in the measurement of volume and temperature in our data we have difficulty applying independent and consistent criteria towards rejecting

individual data points. As a result we are forced to consider each experiment as a whole. The criterion we used for accepting or rejecting a data set is whether it behaved as we expected a solid to within the framework of Birch-Murnaghan and Mie-Guneisen-Debye equations of state. Using this standard we were forced to exclude the GSECARSOS4 data set entirely. In the interest of completeness however, we have appended the data in Appendix A (Table A1).

Figure 3 shows Os volume as a function of pressure for all of the room temperature data. A third-order Birch Murnaghan fit (Birch 1947) to our data set with the V_0 fixed at 27.941 $Å^3$ (Occelli et al. 2004) and K_0' fixed at 4 yields a bulk modulus of 421 (3) GPa. Fits to individual data sets from each beamline and the preheat or quench data agree within two standard deviations. The data are in good agreement with measurements from Kenichi (2004), Occelli et al. (2004), and Voronin et al. (2005).

The high temperature data is shown in Figure 4. Within the resolution of our data, we cannot distinguish among different forms of the high pressure equation of state. Therefore, we use two different approaches to extract the thermoelastic properties of Os: a Mie-Grüneisen-Debye model and a modified high temperature Birch-Murnaghan equation of state (Duffy and Wang 1998). To fit the data set to a Mie-Grüneisen-Debye equation of state we follow the formalism presented in Dorogokupets and Dewaele (2007) where:

$$P(V,T) = P(V,300\ K) + P_{th}(V,T) \quad (1)$$

The isothermal pressure, P(V,300 K), is defined by a third order Birch-Murnaghan equation of state and the thermal pressure $P_{th}(V,T)$ is defined by,

$$P_{th} = \frac{\gamma}{V_{molar}}\left[E_{th} - E_{300K}\right] \quad (2)$$

and,

$$\gamma = \gamma_0 \left(\frac{V}{V_0} \right)^q \quad (3)$$

Where γ_0 is the Grüneisen parameter at ambient conditions, q is a constant proportional to $\frac{d\ln\gamma}{d\ln V}$, V_{molar} is the volume in cm^3/mol, n is the number of atoms per formula unit, R is the universal gas constant, $E_{th} = 3nR\left[\frac{3\theta}{8} + TD\left(\frac{\theta}{T}\right)\right]$, and the Debye function $D\left(\frac{\theta}{T}\right)$ is equal to $3\left(\frac{\theta}{T}\right)^3 \times \int_0^{\frac{\theta}{T}} \frac{z^3 dz}{\left(e^z - 1\right)}$. We solve the Debye function using the high temperature solution of Zharkov and Kalinin (1971) where,

$$D\left(\frac{\theta}{T}\right) = -\frac{3}{8}\left(\frac{\theta}{T}\right) + 3\sum_{k=0}^{\infty} \frac{B_{2k}}{(2k+3)(2k)!}\left(\frac{\theta}{T}\right)^{2k} \quad (4)$$

B_{2k} are Bernoulli numbers and θ is the Debye temperature:

$$\theta(V) = \theta_0 \exp\left[\frac{\gamma_0}{q}\left(1 - \left(\frac{V}{V_0}\right)^q\right)\right] \quad (5)$$

We fix values for osmium's molar volume at ambient conditions to be 8.413 cm^3/mol and the ambient Debye temperature to 477 K. It should be noted that osmium's Debye temperature is poorly constrained but is between 250 and 500 K (Pantea et al. 2008). We adopt Pantea *et al.*'s (2008) value of 477 K although the fit is insensitive to changes in the Debye temperature (a change of 227 K produces a change of 0.03 in the Grüneisen parameter with all other terms fixed). Using a linear least squares regression we find a γ_0 of 2.32 (0.11) and a q of 7.5 (2.1) while fixing V_0 to 27.941 $Å^3$, K_0 to 421 GPa, and K_0' to 4. Fits of individual datasets at high temperature have overlapping 95% confidence intervals. It is worth noting however that each high temperature dataset (HPCATOS3 and ALSOS8) is individually weak at constraining the equation of state. The dataset ALSOS8 has a good spread of temperatures near ambient volume

and gives a much better fit of the ambient Grüneisen parameter than it does of q. Conversely the dataset HPCATOS3 has data spread over a smaller temperature range, but a larger volume range; is gives a better fit of q than it does of the Grüneisen parameter. Residuals between the measured pressure and the pressure predicted by the Mie-Grüneisen-Debye equation of state are plotted in Figure 5.

The second approach is to fit the data to a third-order Birch-Murnaghan equation of state using temperature-modified values of V_0 and K_0 as shown in equations (6) and (7).

$$V_{0T} = V_0 \exp\left(\alpha_0(T - T_0) + \frac{\alpha_1}{2}(T - T_0)^2\right) \quad (6)$$

$$K_0(T) = K_0 + \frac{dK_0}{dT}(T - T_0) \quad (7)$$

Where α_0 is the thermal expansion parameter at ambient conditions, α_1 is its first temperature derivative, and dK_0/dT is the first temperature derivative of the bulk modulus. We assume that K_0' does not vary with temperature (Duffy and Wang 1998). Fixing K_0, K_0', and V_0 to room temperature values we find a dK_0/dT of -0.054 (0.004), an α_0 of 1.48 (0.07)E-5 K^{-1}, and an α_1 of 5.2 (0.8)E-9 K^{-2} (Table 1).

4. Discussion

Our preferred value for thermal expansion and its first temperature derivative at zero pressure are 1.48 (0.07) E-5 K^{-1} and 5.2 (0.8) E-9 K^{-2}. This is in good agreement with values of 1.51 (0.01) E-5 K^{-1} and 5.9 (0.3) E-9 K^{-2} obtained using the same approach from Voronin et al.'s (2005) data. Our value for the temperature derivative of bulk modulus is -0.054 (0.004) GPa/K, also compares favorably with Voronin et al.'s (2005), -0.060 (0.002) GPa/K. Fits of each dataset to a Mie-Grüneisen-Debye model show close agreement as well. We measure a zero pressure

Grüneisen parameter of 2.32 (0.11) and a q of 7.5 (2.2) to Voronin et al.'s (2005) 2.41 (0.02) and 6.7 (0.8). Combining our data set with Voronin et al.'s (2005), we determine a Grüneisen parameter of 2.32 (0.08) and a q of 7.2 (1.4).

The behavior of ultra-hard materials is of significant interest for high temperature applications. One method for predicting and synthesizing ultra-hard materials is to pair a metal with high valence electron density with a lighter element to produce a structure with short covalent bonds (Kaner et al. 2005). For such non-metals, it has been found that bulk modulus and hardness are strongly correlated (Leger and Haines 1997). Predicting the hardness of a metal-based ultra-hard material based on the metal's bulk modulus is an imperfect measure; for example, ReB_2 is harder than OsB_2 despite Re's lower bulk modulus than Os (Zha et al. 2004; Chung et al. 2007; Weinberger et al. 2009). However, the correlation between the bulk modulus and hardness could lead future investigation. Figure 6 shows the relationship between the thermal expansion and the bulk modulus of Os, Re (Zha et al. 2004), and Pt (Matsui et al. 2009) as a function of pressure and temperature. This plot shows that Os metal has the lowest thermal expansion and compressibility of the three elements, especially at high pressures. This trajectory plot provides a graphical distillation of thermoelastic material properties, and can be useful as a design guide for material behavior at extreme conditions.

Since both iron and osmium are in the same elemental group, it has been suggested that the structural behavior of hcp osmium at lower pressures could be an analogue the behavior of iron in the high pressures of Earth's core (Weinberger et al. 2008; Rose et al. 1984). At ambient conditions, the c/a ratio of osmium is 1.581, far below the ideal packing value of 1.633, and our study shows that the c/a ratio increases slightly with both increasing pressure, consistent with earlier work (Cynn et al. 2002; Kenichi 2004; Occelli et al. 2004), and increasing temperature.

Hexagonal close packed iron shows somewhat different behavior. At ambient pressure and temperature, the c/a ratio of iron is equal to 1.603 (Cynn et al. 2002), and this value decreases as a function of pressure and increases with increasing temperature (Cynn et al. 2002; Steinle-Neumann et al. 2001; Ma et al. 2004; Gannarelli and Gillan 2005; Modak et al. 2007). Interestingly, the net result is that the c/a values for iron and osmium show a tendency towards convergence at extreme conditions of high pressures and temperatures. However, actual convergence of these values and possible implications for the Earth's core need to be tested by further experiments.

Table 1: Fitting parameters from the present and previous studies. High temperature data from Voronin et al. (2005) is presented both as derived in that study, and again using our fitting practices. This is done to facilitate a direct comparison between our data sets. Within the thermal Birch-Murnaghan equation of state V_0 is the ambient condition unit cell volume, K_{0T} is the ambient isothermal bulk modulus, K_0' is the first pressure derivative of the bulk modulus, α_0 is the ambient thermal expansion parameter, α_1 is the first temperature derivative of thermal expansion, and dK/dT is the first temperature derivative of bulk modulus. In the Mie-Grüneisen-Debye equation of state γ_0 is the ambient Grüneisen parameter and q is a constant proportional to $\frac{d\ln\gamma}{d\ln V}$.

Sources	V_0 (Å^3)	K_{0T} (GPa)	K_0'	α_0 (E-5 K^{-1})	α_1 (E-9 K^{-1})	dK_0/dT (GPa/K)
Cynn 2002	27.956	462 (12)	2.4 (0.5)			
Kenichi 2004	27.977	395 (2)	4.5 (1)			
Occelli 2004	27.941 (0.008)	411 (6)	4.0 (0.2)			
Voronin 2005	27.931 (0.005)	435 (19)	3.5 (0.8)			-0.060 (0.010)
Pantea 2009		405 (5)				
Our results Isothermal EoS	27.941 (fixed)	421 (3)	4 (fixed)			
Isothermal EoS	27.941 (fixed)	421 (3)	4 (fixed)			
Thermal EoS Our dataset	27.941 (fixed)	421 (fixed)	4 (fixed)	1.48 (0.07)	5.2 (0.8)	-0.054 (0.004)

Thermal EoS Voronin	27.931 (fixed)	435 (fixed)	3.5 (fixed)	1.51 (0.01)	5.9 (0.3)	-0.060 (0.002)
Thermal EoS combined dataset[1]	27.941 (fixed)	421 (fixed)	4 (fixed)	1.51 (0.06)	4.9 (0.7)	-0.055 (0.004)
Source	V_0 (Å^3)	K_{0T} (GPa)	K_0'	γ_0	q	-
MGD EoS Our dataset	27.941 (fixed)	421 (fixed)	4 (fixed)	2.32 (0.11)	7.5 (2.2)	
MGD EoS Voronin	27.931 (fixed)	435 (fixed)	3.5 (fixed)	2.41 (0.02)	6.7 (0.8)	
MGD EoS combined dataset[1]	27.941 (fixed)	421 (fixed)	4 (fixed)	2.32 (0.08)	7.2 (1.4)	

[1] refers to joint dataset of our results and Voronin's

Table 2: Summary of experimental conditions

Experiment	X-ray wavelength (Å)	Beamsize (μm)	Laser FWHM (μm)	Compressed gasket thickness (μm)	Pressure standard	Pressure medium	Pressure range (GPa)	Temperature range (K)
ALSOS3	0.4959	10x10	30	30	NaCl	NaCl	7-51	300
ALSOS8	0.4133	10x10	30	50	NaCl	NaCl	7-18	300-2873
HPCATOS3	0.3706	7x8	30	30	MgO	Ne	6-46	300-2769
GSECARSOS4	0.3344	5x5	25	30	MgO	Ne	22-47	300-2440

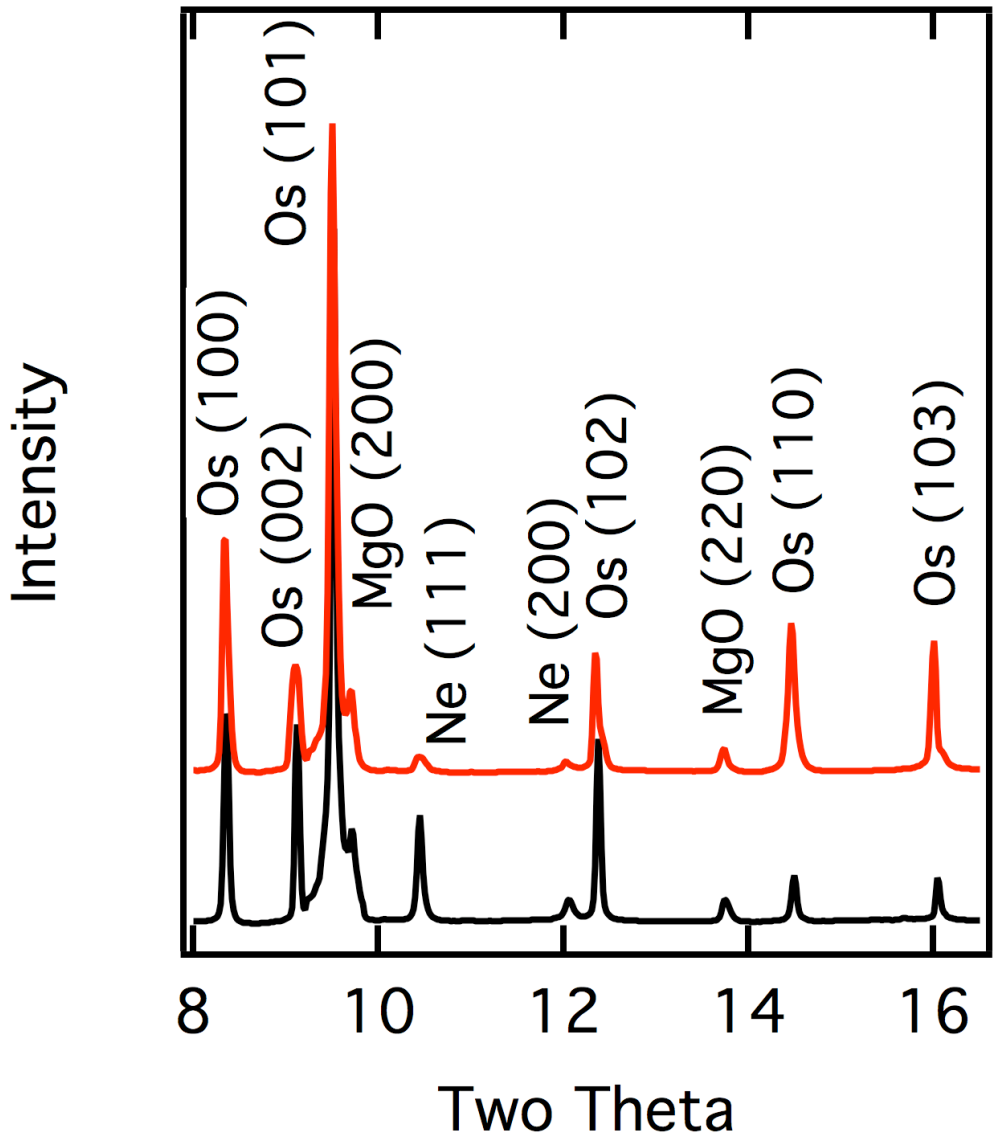

Figure 1. Representative diffraction patterns of Os at room temperature (black) and at high temperature (~2000 K) (gray). Diffraction peaks of osmium (Os), periclase (MgO), and neon (Ne) are marked.

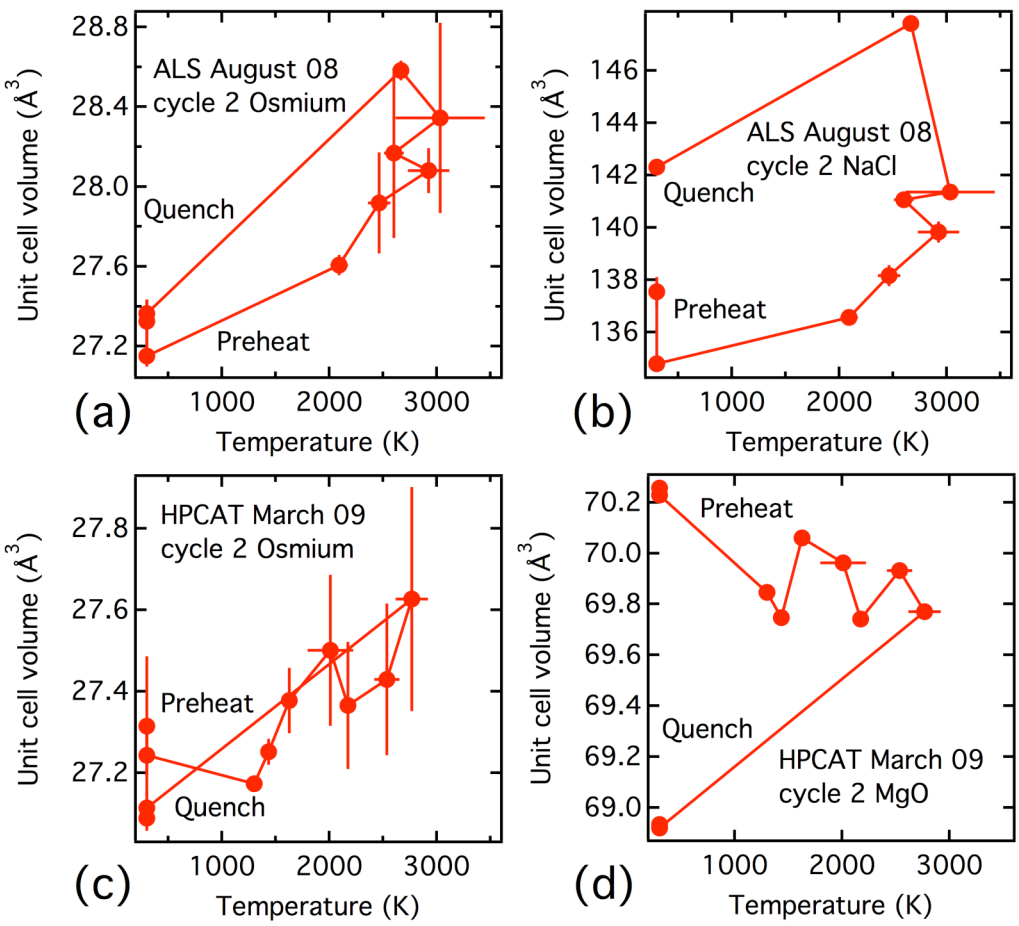

Figure 2. Measured volume-temperature cycles for Os and pressure calibrant for two representative heating cycles. a) Osmium and b) NaCl volume vs. Temperature corresponding to ALSOS08 cycle 2. c) Osmium and d) MgO volume vs. temperature, corresponding to HPCATOS3 cycle 5. Volumes obtained during preheat and quench are labeled.

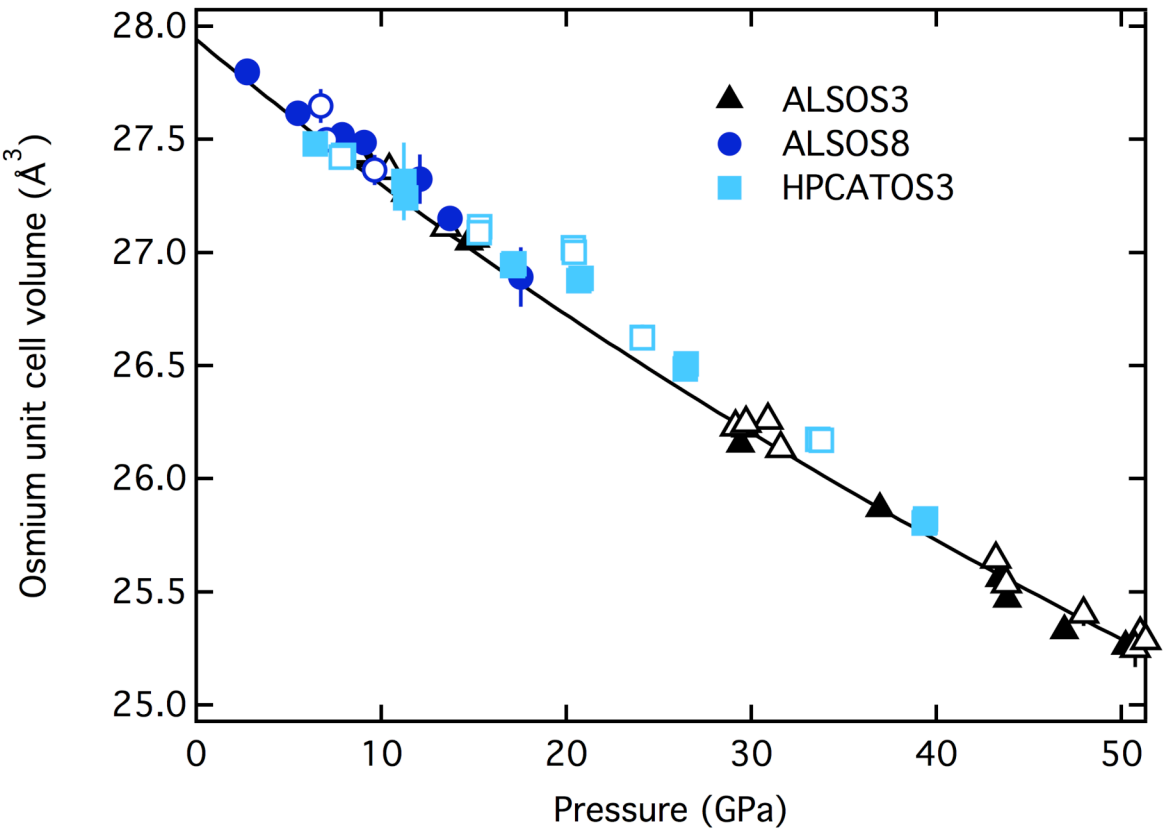

Figure 3. Room temperature osmium unit cell volumes plotted as a function of pressure. The datasets ALSOS3 (triangles) and ALSOS8 (circles) used the NaCl B1 and NaCl B2 pressures scales while the dataset HPCATOS3 (squares) used the MgO pressure scale. Closed symbols indicate preheat measurements and open symbols indicate quenched measurements. Fitting the data to a third order Birch-Murnaghan equation of state gives a bulk modulus of 421 (3) GPa with a zero pressure volume fixed at 27.941 Å^3 (Occelli et al. 2004) and a first pressure derivative fixed at 4. The published equation of state of Occelli et al. (2004; line) is appended for reference.

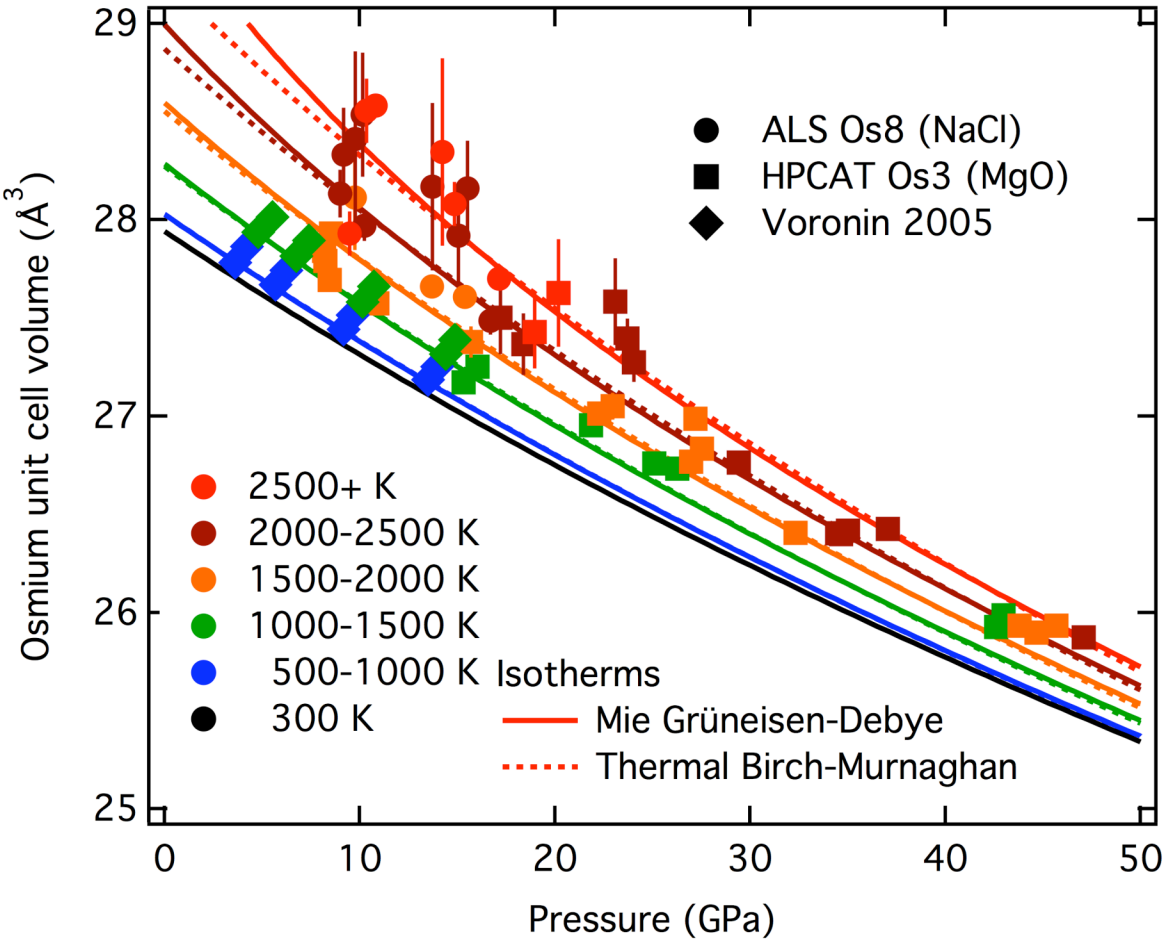

Figure 4. The high temperature data we used to constrain the high temperature equation of state comes from the datasets ALSOS8 (circles) and HPCATOS3 (squares). Data from Voronin et al. (2005; diamonds) is included for comparison. Measurements are binned into temperature ranges as described in the inset. High temperature equations of state are calculated with respect to the best fit to the ambient temperature equation of state (black line). Calculated isotherms are appended for reference and color coded to the lower end of the corresponding temperature range. Isotherms are calculated using either the Mie-Grüneisen-Debye (solid lines) equation of state or a thermal Birch-Murnaghan equation of state (dotted lines).

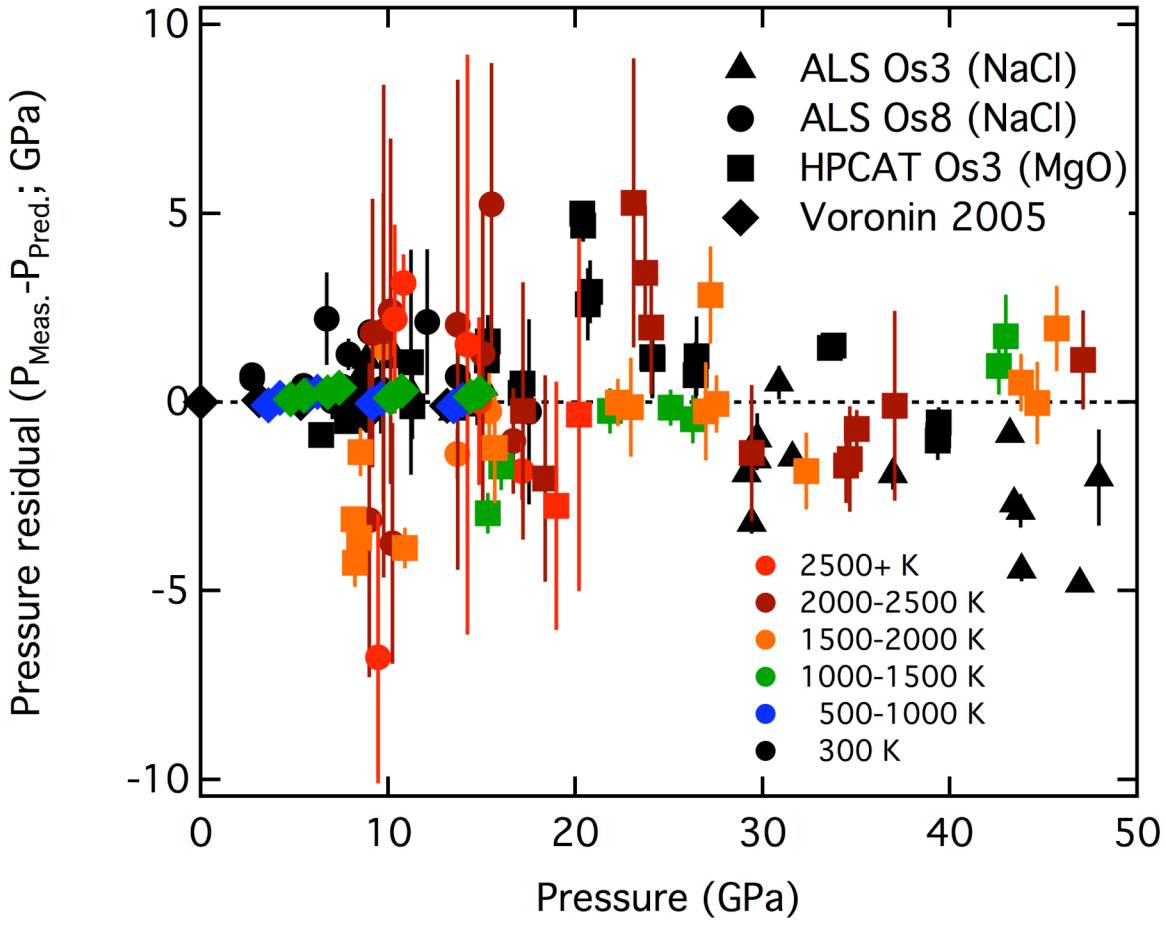

Figure 5. Pressure residuals from Figures 3 and 4. Residuals are calculated as the difference between measured pressures and pressures predicted by the Mie-Grüneisen-Debye equation of state. Error bars show 1σ uncertainties.

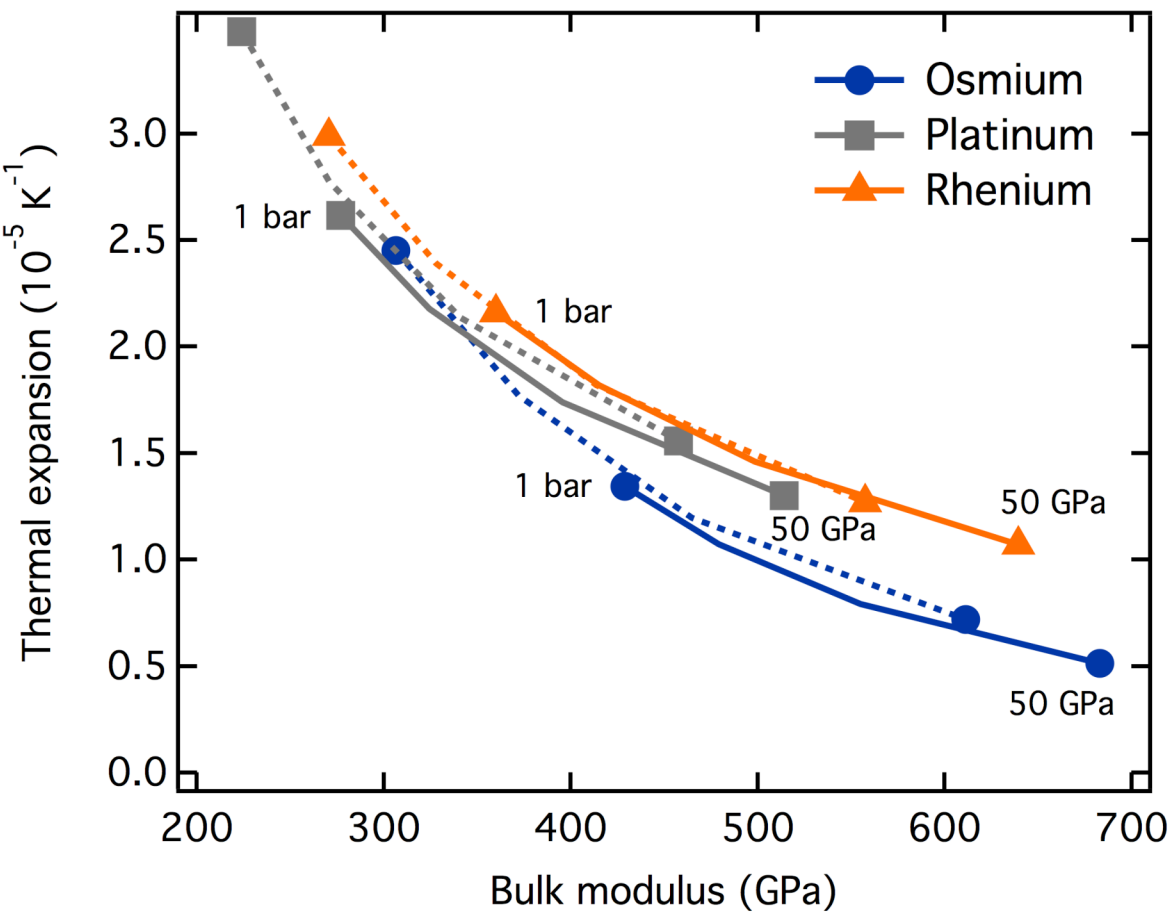

Figure 6. The thermal expansion of platinum (squares), rhenium (triangles), and osmium (circles) is plotted as a function of their bulk moduli. Solid lines are values at 300 K and dotted lines are values at 2000 K. The curves represent values for pressures from 0 GPa (at left) to 50 GPa (at right). Osmium generally has lower thermal expansion and higher bulk modulus than both platinum and rhenium.

High Pressure, High Temperature Equation of state for Fe_2SiO_4 ringwoodite and implications for the Earth's transition zone.

Abstract

We measured the density of iron-ringwoodite and its pressure and temperature dependence at conditions of the mantle transition zone using the laser-heated diamond anvil cell in conjunction with X-ray diffraction. Our new data combined with previous measurements constrain the thermoelastic properties of ringwoodite as a function of pressure and temperature throughout the transition zone. Our best fit Mie-Grüneisen-Debye equation of state parameters for Fe end-member ringwoodite are K_0 = 202 (4) GPa, $K' = 4$, γ_0 = 1.08 (6), q = 2, and θ_D = 685 K. This new equation of state revises calculated densities of the Fe end-member at transition zone conditions upwards by ~0.6% compared with previous formulations. We combine our data with equation of state parameters across the Mg-Fe compositional range to quantify the effect of iron and temperature on the density and bulk sound velocity of ringwoodite at pressure and temperature conditions of the Earth's transition zone. The results show that variations in iron content and temperature have opposing effects on density and bulk sound velocity, suggesting that compositional (iron content) and temperature variations in the transition zone may be distinguished using seismic observables.

1. Introduction

Measurements of equation of state parameters for minerals of the mantle's transition zone at relevant high pressures and temperatures provide the key to interpret seismic observations in terms of composition and temperature. Seismic tomography studies have parameterized lateral variations in travel time with variations in iron content, silica content, and temperature (e.g. Trampert et al. 2004). However these studies have been limited in part by the lack of tightly constrained equation of state parameters for relevant minerals and conditions. Ringwoodite $(Mg,Fe)_2SiO_4$ is the spinel-structured polymorph of olivine and likely the predominant mineral in the deep part of the transition zone (Hirose 2006). While many measurements exist for the high pressure, high temperature equation of state at transition zone conditions at and close to the Mg end-member, only a small suite of measurements exist for Fe-ringwoodite (e.g. Mao et al. 1969; Suzuki 1979; Hazen 1993; Plymate and Stout; 1994 Nishihara et al. 2004; Liu et al. 2008) and none of these are at the pressures and temperatures of the transition zone. Significant uncertainties are introduced by extrapolating these results to relevant high pressures and temperatures, and therefore the effect of iron on the density and bulk modulus of ringwoodite is not well-constrained at the conditions of the transition zone. Our approach is to measure the density of Fe end-member ringwoodite using synchrotron X-ray diffraction techniques combined with laser heating in the diamond anvil cell. Together with previous measurements across the ringwoodite compositional range, our new equation of state allows interpretation of the seismic observations, both global and local, in terms of iron content and temperature.

2. Methods

Fe-ringwoodite was synthesized in the laser-heated diamond anvil cell from a single-crystal fayalite starting material that had been polished to a thickness of ~30 μm. A crystal

approximately ~50 μm x 50 μm was loaded into a diamond anvil cell equipped with 500 μm culets, and a precompressed rhenium gasket with a sample chamber drilled to a diameter of ~150 μm. The sample was loaded between two ~10 μm plates of NaCl, which served as thermal insulators from the diamonds, as a pressure calibrant, and pressure medium. Powder diffraction measurements of ringwoodite and NaCl in the laser-heated diamond anvil cell were obtained at the ID-D beamline of GSECARS at the Advanced Photon Source at high pressures and temperatures. A monochromatic x-ray beam of wavelength 0.3344 Å was used for all diffraction measurements, and angle-dispersive X-ray diffraction patterns were collected using a MAR imaging system. Exposure times were generally ~30 seconds. Two heating cycles were performed at successively higher pressures, each consisting of a series of diffraction patterns obtained before, during, and after laser heating. Laser heating of both sides of the sample was performed using an infrared fiber laser split and beamed through each diamond anvil (Prakapenka et al. 2008). Spectral intensity data from the laser heated spots on each side was collected throughout heating, and temperature measurements were made by fitting the spectral intensity to a Planck radiation curve. The superposition of the X-ray beam (~10x10 μm) and the laser heated spot (~20 μm FWHM) was established by imaging NaCl's fluorescence under the X-ray beam, and comparing it to the position of the laser-heated spot before and after each heating cycle. Fluorescence could not be monitored during the high temperature portion of the cycle. However, if concordance of the fluorescent (X-ray) spot and thermal hotspot position were not established both before and after the heating cycle, the data was not used during the analysis.

Two-dimensional diffraction patterns were integrated using the software package Fit2D (Hammersley et al. 1996), and the NaCl and Fe_2SiO_4 ringwoodite peaks were indexed (Figure 7). NaCl lattice parameters were determined using Gaussian fits to the (111), (200), (220), (222),

and (400) diffraction peaks. Ringwoodite's lattice parameter was determined using the (220), (311), (222), (400), (422), (511), (440), (531), (620), (533), (622), and (551/711) indices (Appendix A, Table A2). Error bars on the lattice parameter were obtained by calculating the standard deviation of the average lattice parameter values. Pressure was obtained by referencing the high pressure, high temperature equation of state of NaCl (Brown 1999). Because of strong axial temperature gradients in the diamond cell, it is likely that the average temperature experienced by the NaCl volume that is sampled by X-rays is significantly different from the ringwoodite temperature. Since NaCl acts as a thermal insulating layer between the diamond surface and the hotspot, following Seagle et al. (2008), we infer the temperature of the X-rayed volume of the NaCl to be halfway between the hotspot temperature and 300 K temperature of the diamond. Typical errors in pressure measurement arising from lattice parameter variations are ~0.25-0.5 GPa. A ~200 K temperature error translates to a pressure error of ~0.5 GPa. However, because temperature errors are likely to be systematic, the results for the high P,T EoS parameters are insensitive to small systematic pressure errors.

3. Results

Our complete data set showing measured volumes as a function of pressure and temperature is plotted in Figure 8. As a first step we performed a linear least squares fit to the previous room temperature data (Sato 1977**;** Wilburn and Bassett 1976; Liu et al. 2008; Nestola et al. 2010) to determine the tradeoff between the correlated parameters K_0 and K′, with the best fit result determined by the relationship $K_0 = 214.3\text{-}3.2K'$ and preferred values of K_0=202 (4) GPa and with K′ fixed at 4. The room temperature data anchor the high P,T equation of state. Combining our data sets with those of Liu et al. (2008) and Plymate and Stout (1994) we calculated a best fit high temperature equation of state using a Mie-Grüneisen-Debye formalism

(Dorogokupets and Dewaele 2007). The thermal parameters of the Grüneisen parameter γ and q are also strongly correlated, and due to the narrow pressure range of the data, the q parameter is not well constrained. For q values of 1, 2, and 3, the best fit Grüneisen parameters are 1.06 (6), 1.08 (6), and 1.10 (6) respectively. These different sets of equation of parameters generate virtually indistinguishable densities and elastic properties for iron ringwoodite at transition zone conditions. Our preferred fit to the total high P,T data set for Fe end-member ringwoodite is a Grüneisen parameter (γ_0) of 1.08 (6) and q fixed to 2, holding the Debye temperature (θ_0) constant at 685 K (Stixrude and Lithgow-Bertelloni 2005). Residuals between the predicted and measured pressure are plotted in Figure 9. This revised equation of state gives somewhat higher densities than Stixrude and Lithgow-Bertelloni (2005) and Liu et al. (2008).

4. Discussion

Combining our newly refined high pressure high temperature equation of state for iron ringwoodite with previously existing data on the magnesium end-member we plot density, bulk modulus and bulk sound velocity of ringwoodite as a function of iron content at pressures at the top and bottom of the transition zone and at high (1500 K) and low (300 K) temperatures (Figure 10). Calculations are done as a linear average between our iron end-member ringwoodite and the magnesium end-member reported by Stixrude and Lithgow-Bertelloni (2005). Figure 11 shows the sensitivity of transition zone density (11a) and bulk sound velocity (11b) to variations in temperature and iron content. The calculations are performed with respect to a $(Mg_{0.85}Fe_{0.15})_2SiO_4$ composition at the pressure and temperature conditions corresponding a geotherm rooted at 1694 K at 410 km depth (Brown and Shankland 1981). Ultimately more complicated mineral assemblages including wadsleyite and majorite need to be considered.

However, these mineralogical phases show similar qualitative behavior in how their density and bulk moduli vary with changes in iron content and temperature. Our calculations show that density is more sensitive to perturbations in iron content while bulk sound velocity is more sensitive to changes in temperature. Variations in iron content and temperature have different effects, both in magnitude and sign, on density and bulk sound velocity. In detail, sensitivity of seismic observations relies on a tradeoff between the magnitude of the signal and its lateral extent, and likely varies strongly with depth (Romanowicz 2003; Masters and Gubbins 2003; Trampert et al. 2004). As a starting point for examining how our results compare with typical seismic resolutions, we choose values of 0.5% in density, and 0.2% in velocity, roughly corresponding to estimates for spatial resolutions of 200-300 km in the transition zone.

Our results predict changes in seismic observables that result from coupled thermal and compositional anomalies (Figure 12). For example, an iron-rich, hotter-than average upwelling through the transition zone will significantly decrease bulk sound velocity, while the density perturbation is minimal due to the opposing effects of iron and temperature (all other things being equal). On the other hand, a subducting slab likely has lower temperatures and higher iron content compared with surrounding mantle. In this case, the density is predicted to increase while the bulk sound velocity effect is minimized. Interestingly the effects of iron and temperature on density and bulk modulus oppose each other (Figure 12), suggesting that these effects may be independently resolvable.

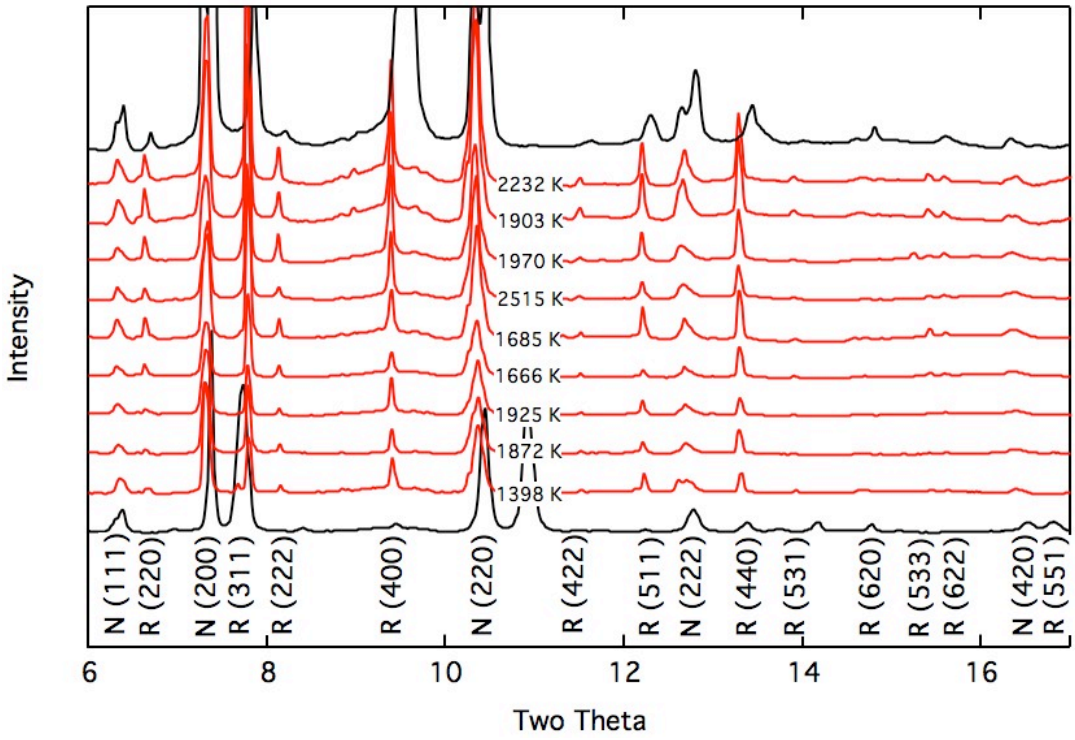

Figure 7. X-ray diffraction patterns obtained during heating cycle 2 (~11 GPa). The preheat and quench patterns are shown in black. The patterns in red were obtained during laser heating. Diffraction peaks from both NaCl (N) and Ringwoodite (R) are labeled.

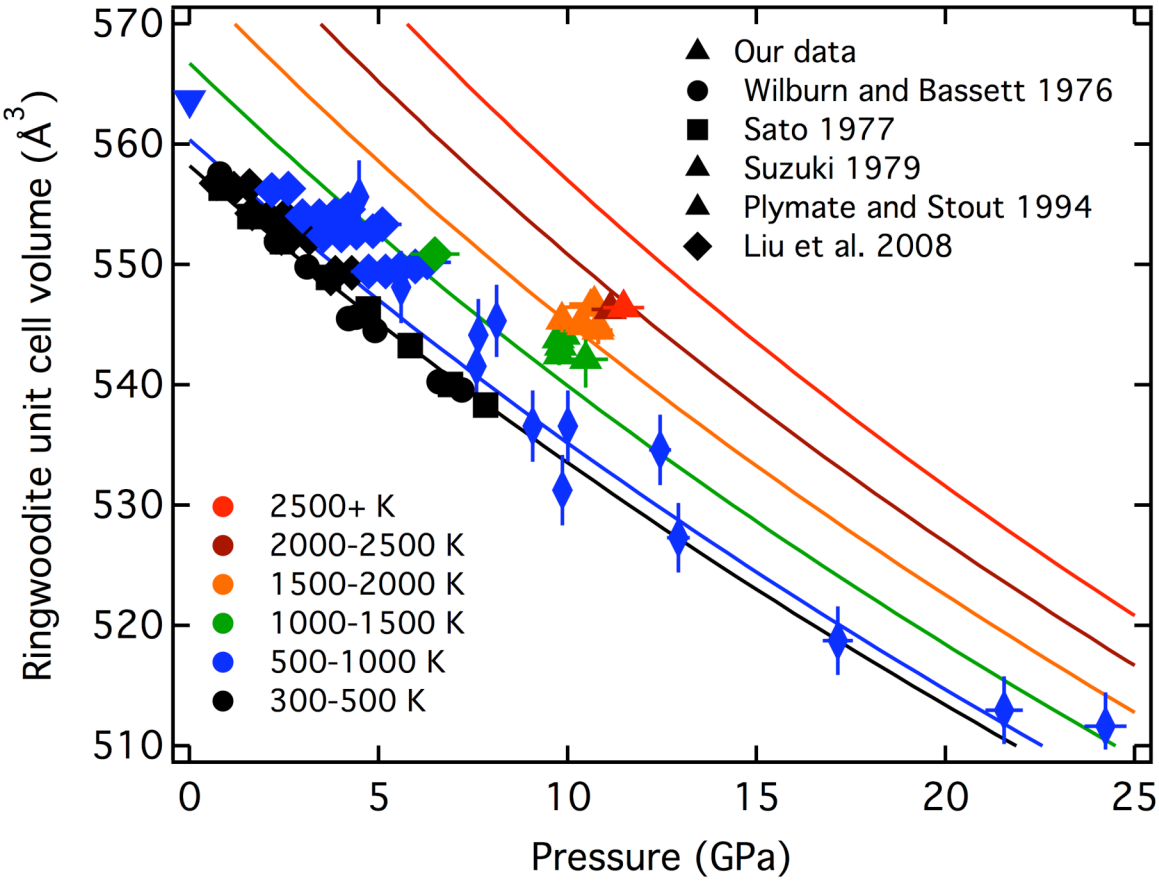

Figure 8. Plot of unit cell volume versus pressure for all data. Data is binned by temperature as described in the inset. Best fit isotherms are plotted for the lower end of each temperature bin.

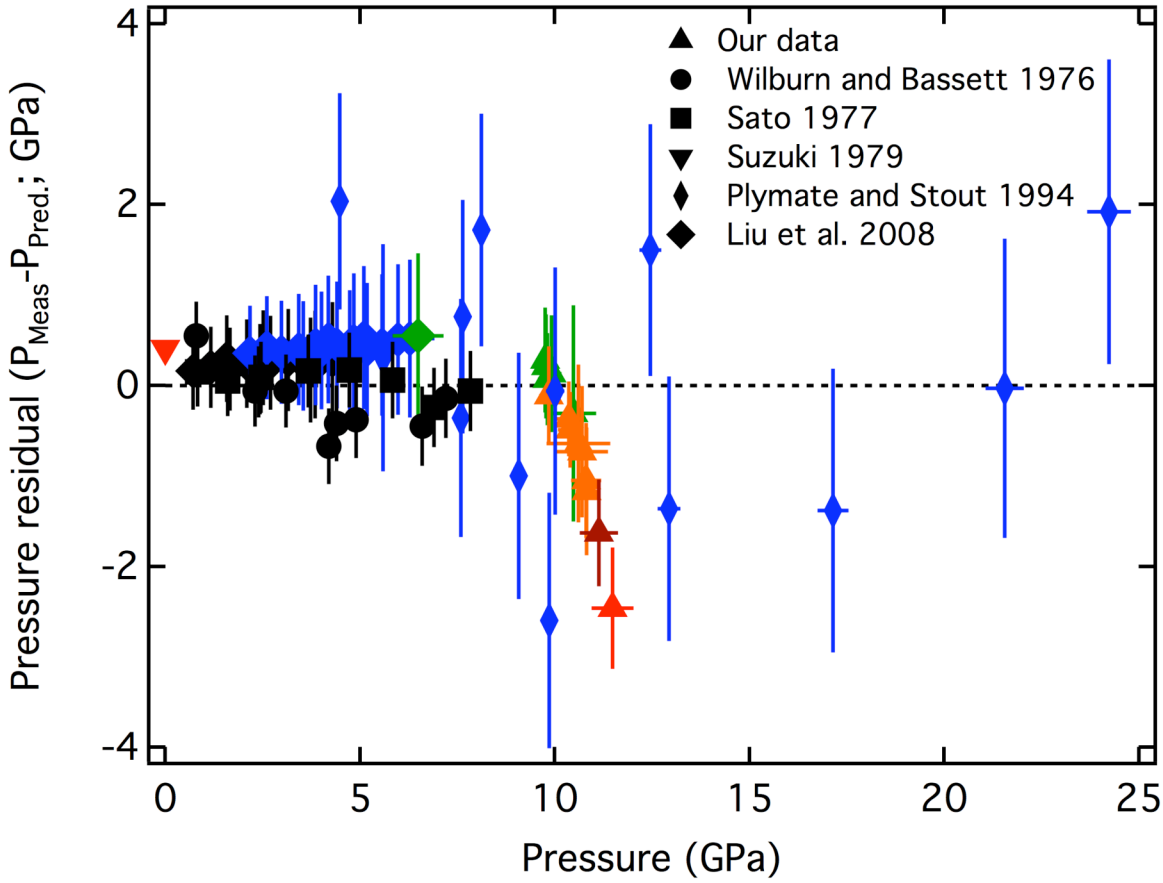

Figure 9. Pressure residuals for all data in Figure 8. Residuals are plotted as the difference between the measured pressure and the pressure predicted by the equation of state. Measurements are binned by temperature as in Figure 8. Our measurements show a strong trend with temperature. Measurements up to ~1500 K are in good agreement with the equation of state, but higher temperature measurements have systematically lower than predicted pressures.

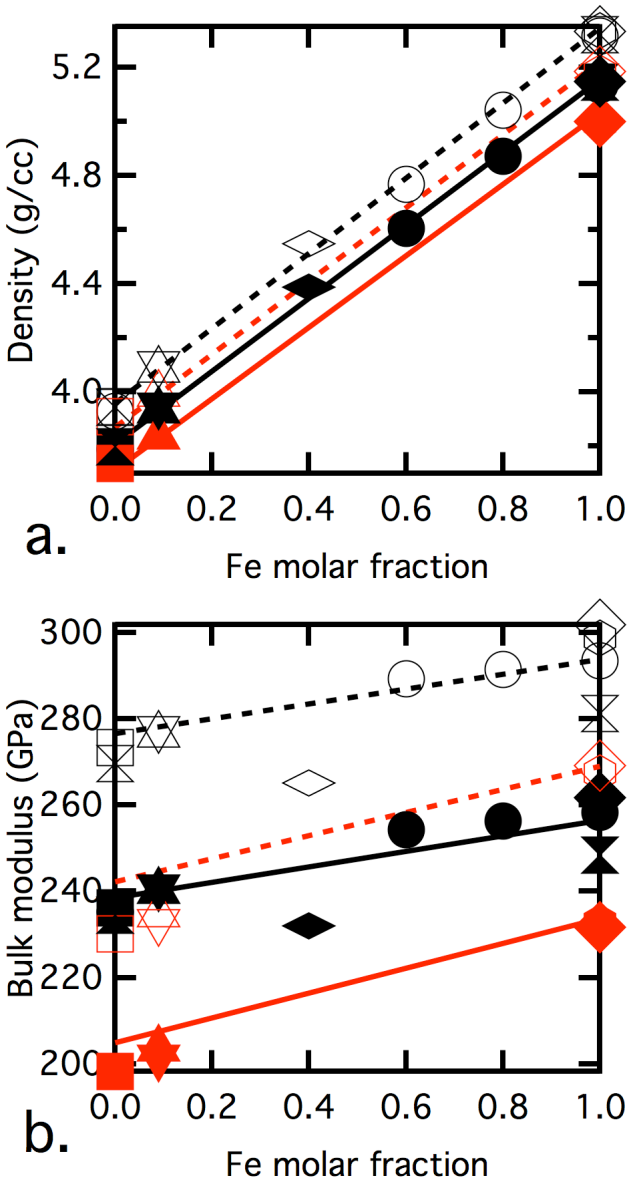
5.2
4.8
4.4
4.0
Density (g/cc)
0.0
0.2
0.4
0.6
0.8
1.0
Fe molar fraction
a.
300
280
260
240
220
200
Bulk modulus (GPa)
0.0
0.2
0.4
0.6
0.8
1.0
Fe molar fraction
b.

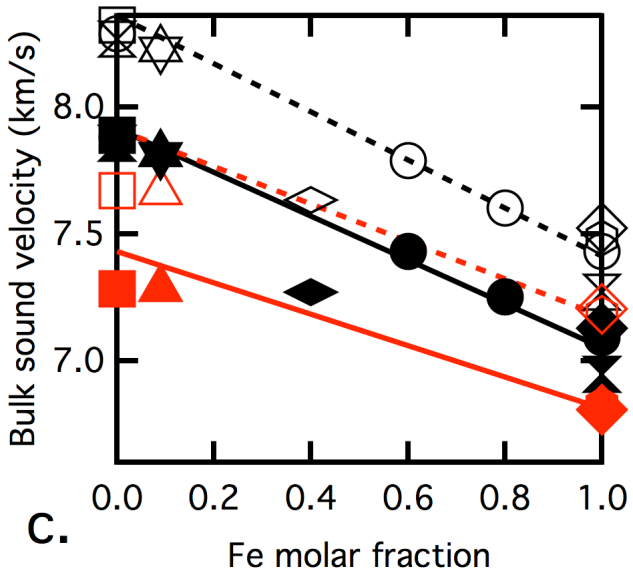

Figure 10. Ringwoodite Equation of state data as a function of iron content. **(a.)** A plot of the density of ringwoodite at high pressure and temperature as a function of iron content. Calculations are performed as a linear average of our iron end-member results and the Mg end-member reported by Stixrude and Lithgow-Bertelloni (2005). Densities are reported at 300 K (black) and at high temperature (red, corresponding to projected temperatures at the top and bottom of the transition zone (Brown and Shankland 1984)). Solid lines and dotted lines are densities calculated at the top (14 GPa) and bottom (24 GPa) of the transition zone, respectively. Values from the literature are plotted using the same color convention, and with closed and open symbols corresponding to 14 GPa and 24 GPa respectively. Legend: Kuskov (1984; hexagons), Rigden and Jackson (1991; hourglasses), Hazen (1993; circles), Meng et al. (1994; squares), Zerr et al. (1994; oblate diamonds), Sinogeikin and Bass (2001; inverted triangles), Nishihara et al. (2004; upright triangles), and Liu et al. (2008; diamonds). **(b.)** The bulk modulus of ringwoodite at high pressure and temperature as a function of iron content. (**c.)** The bulk sound velocity of ringwoodite at high pressure and temperature as a function of iron content.

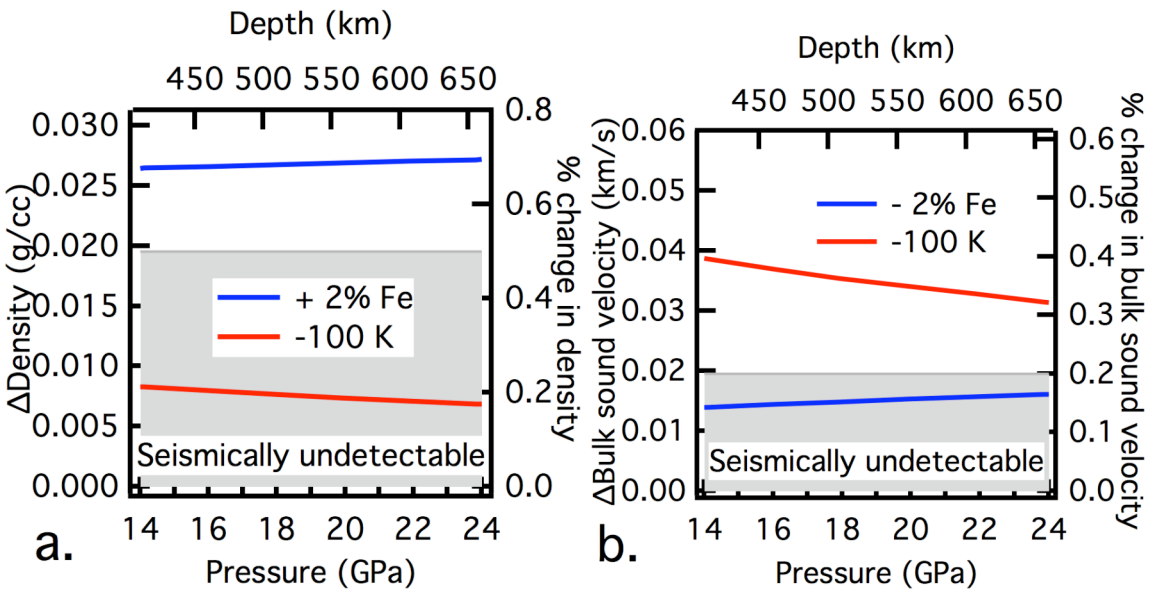

Figure 11. (a) Density change with iron content and temperature as a function of pressure along a transition zone geotherm rooted at 1694 K at 410 km (Brown and Shankland 1981). The base composition is assumed to be $(Mg_{0.85}Fe_{0.15})_2SiO_4$ ringwoodite. The percent change is referenced to the value at 410 km depth. A threshold of seismic visibility at a resolution of 200 km is appended for reference. **(b)** Change in bulk sound velocity with iron content and temperature as a function of pressure along a geotherm.

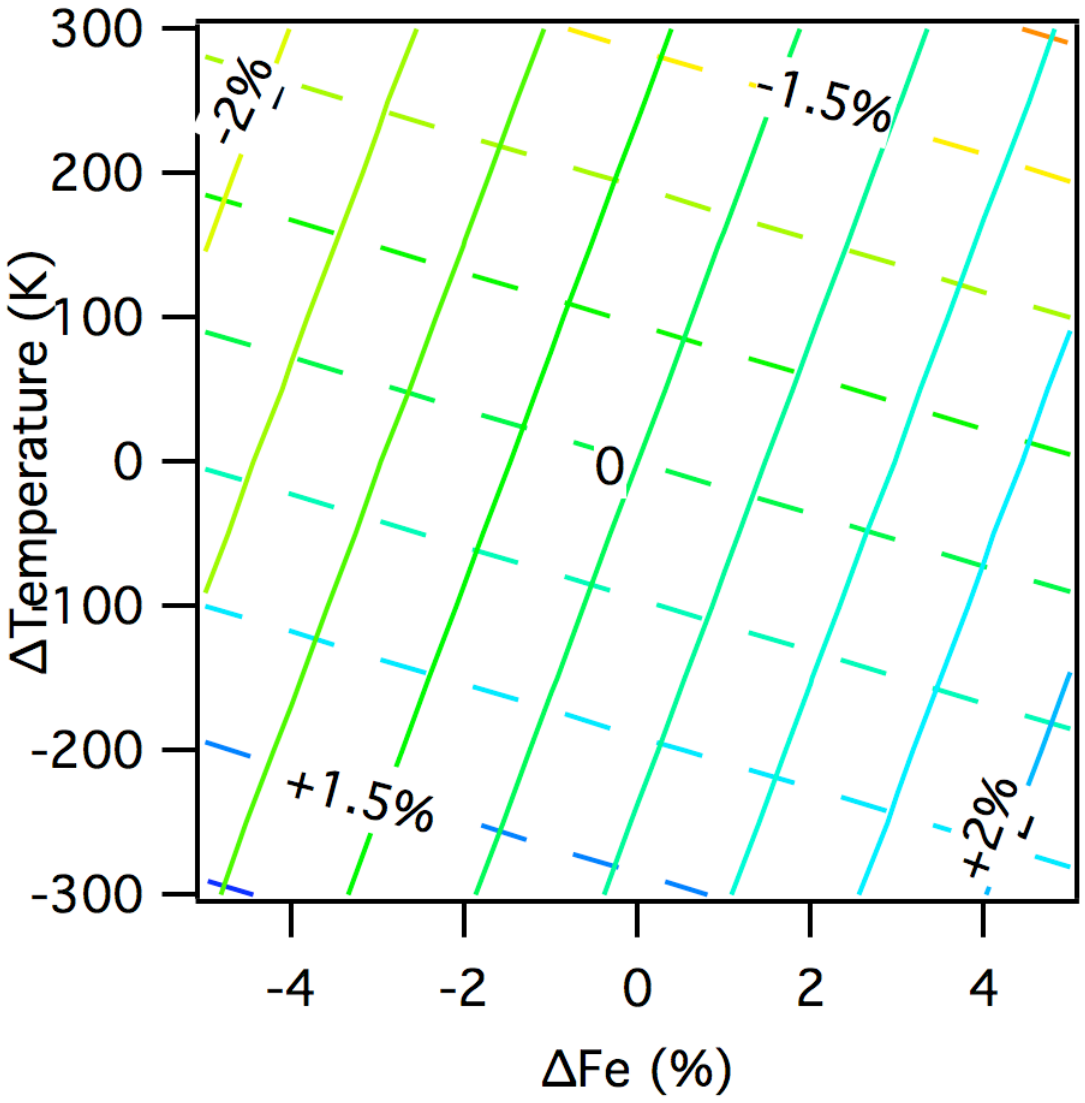

Figure 12. Schematic representation of the effect of changes in composition and temperature on ringwoodite's density (solid) and bulk sound velocity (dashed). Contours of density and bulk sound velocity are plotted in increments of 0.5% difference from 410 km reference values. Different combinations of thermal and compositional anomalies have distinct seismic signatures since the effect of iron and temperature on density and bulk sound velocity oppose each other.

Phase relations and equation of state in the cobalt oxide system: Implications for redox relations in Earth's mantle

Abstract

The phase stability and high pressure and temperature equation of state of cobalt oxide was measured up to 65 GPa and 2600 K. We find that the rocksalt structure is stable relative to the rhombodedral phase at high temperature throughout the study. Fitting a Mie-Grüneisen-Debye model to the B1 data we find best fit parameters V_0=77.4 (fixed) $Å^3$, K_0=190 (1) GPa, K´=3.49 (4), γ_0=1.54 (4), q=2.87 (15), and θ_0=517.8 (fixed). We use this newly determined equation of states in conjunction with existing thermoelastic parameters of cobalt metal to extend the CoO/Co oxygen fugacity buffer to high pressures and temperatures and to predict relative redox behavior in the deep Earth.

1. Introduction

The equations of state and phase relations of transition metal oxides provide insight into the electronic behavior of these highly correlated solids. In addition, the thermodynamic behavior of metal-oxide systems at high pressures and temperatures constrains the formation and evolution of the core mantle system, which is itself a metal-oxide interface. The relative partitioning behavior of cobalt, nickel, and iron in particular have been used to predict the conditions of an early core mantle boundary (Kegler et al. 2008; Li and Agee 1996; O'Neill et al. 1998; Righter 2003). Interpreting this geochemical information requires knowledge of the phase stability and equation of states of these elements in their metallic and oxide states. While equation of state measurements exist for the iron and nickel systems (Campbell et al. 2009), cobalt oxide has not been studied at high pressures and temperatures. In this study we use the laser heated diamond anvil cell in conjunction with synchrotron X-ray diffraction to measure the phase stability and equation of state of cobalt oxide at conditions of the lower mantle.

At ambient conditions cobalt oxide assumes the paramagnetic rocksalt structure. Like several other transition metal oxides it undergoes a slight combined rhombohedral and tetragonal distortion to an antiferromagnetic phase below the Néel temperature and at 1 bar (Wdowik and Legut 2008; Roth 1958; Shull et al. 1951). A similar distortion is observed at 43 (2) GPa and ambient temperature (Guo et al. 2002), although it is unknown whether it is the same as the lower pressure rhombohedral phase. At 90-97 GPa there is a volume collapse that is associated with a high to low spin transition similar to ferropericlase (Guo et al. 2002; Rueff et al. 2005; Zhang et al. 2009).

The compressibility of the rocksalt phase has been measured both by ultrasonic (Sumino et al. 1980.) and static (Guo et al. 2002) methods and its ambient pressure thermal expansion has

been measured (Massobrio and Meyer 1991; Touzelin 1978). However a simultaneous high pressure and temperature determination of the equation of state of cobalt oxide is lacking. These measurements provide important constraints on the understanding of metal oxides at extreme conditions and the thermodynamics of metal-oxide equilibria in the deep Earth.

2. Experimental Methods

High pressure and temperature lattice parameter measurements were performed using the laser heated diamond anvil cell with 200 μm culets and synchrotron X-ray diffraction. A rhenium gasket was pre-indented to a thickness of 20 μm and drilled to a diameter of 90 μm. Cobalt oxide powder with a grain size of <5 μm was pressed into a plate ~ 5 μm thick and loaded between two ~8 μm plates of dry powdered NaCl, which functioned as pressure medium, thermal insulator, and pressure standard.

Samples were heated using a double-sided fiber IR laser system (Prakapenka et al. 2008). Multiple temperature measurements were obtained from each side of the sample using the emitted Planck radiation during each X-ray exposure, with good agreement on each side indicating symmetric insulation. We report the mean value of 2 to 12 temperature measurements along with their standard deviations, which are generally less than 5% indicating good temporal stability.

A total of twenty heating cycles were performed on a single sample between 6 and 65 GPa. X-ray diffraction patterns were obtained before, during, and after each heating cycle using the GSECARS CCD imaging system with an X-ray spot size of ~5x5μm and wavelength of 0.3344 Å. Sample to detector distances were calibrated using a CeO_2 standard. Intensity vs. two-theta X-ray diffraction patterns were generated from the two-dimensional image using the

software Fit2D (Hammersley et al. 1996). The coaxial alignment of X-ray volume and laser hotspot is crucial for interpretation of high-pressure, high-temperature diffraction data (Kavner and Panero 2004). Alignment was confirmed before and after each heating cycle using the visible X-ray fluorescence of NaCl. The alignment was found to be consistent within 5 microns before and after each heating cycle.

Diffraction patterns were indexed, and individual *d*-spacings determined by a Gaussian fit to each diffraction peak (Figure 13). In each diffraction pattern, the lattice parameter of cobalt oxide was determined from the (111), (200), and (220) *d*-spacings. The corresponding lattice parameter of the NaCl B1 structure was determined using the (111), (200), (220), (311), (222), (400), and (420) peaks and the lattice parameter of the NaCl B2 structure was determined using the (100), (110), (111), (200), and (210) diffraction peaks.

We determine the high P,T equation of state of cobalt oxide with respect to the established equations of state of the B1 and B2 structures of NaCl (Dorogokupets and Dewaele 2007). Because NaCl acts as a thermal insulator between the laser-heated samples and the diamonds, we assume that the temperature of NaCl is halfway between the measured temperature of the sample and 300 K. In patterns that have both the B1 and B2 structures of NaCl present we find agreement between the inferred pressures within 1 GPa.

Ambient temperature diffraction measurements exhibit significant strain anisotropy (Figure 13a) that disappears upon heating (Figure 13b). For this reason we omit our ambient temperature measurements from our analysis. Lattice parameters of cobalt oxide and NaCl, average temperatures, and inferred pressures are listed in Table A3 in Appendix A.

3. Results

3.1 Phase stability

The ambient temperature phase diagram of cobalt oxide has been characterized up to >1 Mbar at room temperature (Guo et al. 2002; Rueff et al 2005). In this range there are two phase transitions: from the cubic B1 structure to a rhombohedral structure at 43 (2) GPa (Guo et al 2002), and from the rB1 structure to a higher density rhombohedral structure between 90 and 97 GPa (Guo et al. 2002; Rueff et al. 2005). The maximum pressure of our experiments is ~65 GPa, so we potentially expect to see the rB1 phase, but not the high pressure rhombohedral phase.

The identification of the rB1 phase is problematic. The symmetry of the rB1 phase is $R\bar{3}m$ (Wdowik and Legut 2008) and is characterized by a slight distortion of the B1 unit cell in the [111] direction. The metric for identifying the phase change is the appearance of a low intensity shoulder on the (111) peak and a splitting of the (220) peak. However, this feature is subtle since the angular distortion is much less than 1% (Wdowik and Legut 2008; Roth 1958; Shull et al. 1951). We do not observe splitting of either the (111) or (220) lines within any of our high temperature patterns. Additionally there is no abrupt change in the goodness-of-fit to the cubic structure with increasing pressure. For this reason we suspect that the B1 to rhombohedral phase transition may have a shallow Clapeyron slope that makes it unstable at high temperatures, similar to the analogous phase transition in FeO (Murakami et al. 2004). However it is also possible that we do observe the rhombohedral phase, but the difference is below the detection threshold.

3.2 High temperature equation of state

High pressure and temperature equations of state are constructed using a reference isotherm combined with a thermal pressure correction.

$$P(V,T) = P_{300K}(V) + P_{th}(V,T) \quad (8)$$

We use a Birch-Murnaghan isothermal reference equation of state (Birch 1947).

$$P_{300K}(V) = 1.5K_{0T}\left[\left(\frac{V}{V_0}\right)^{-\frac{7}{3}} - \left(\frac{V}{V_0}\right)^{-\frac{5}{3}}\right]\left[1 + \frac{3}{4}\left(K' - 4\right)\left(\left(\frac{V}{V_0}\right)^{-\frac{2}{3}} - 1\right)\right] \quad (9)$$

where V_0 is the ambient pressure unit cell volume, K_{0T} is the ambient isothermal bulk modulus and K′ is its first pressure derivative, evaluated at P=0. We use the Mie-Grüneisen-Debye model to constrain a thermal pressure,

$$P_{th}(V,T) = \frac{\gamma}{V}3nk\left[T\int_0^{\frac{\theta}{T}}\frac{z^3 dz}{\left(e^z - 1\right)} - 300K\int_0^{\frac{\theta}{300K}}\frac{z^3 dz}{\left(e^z - 1\right)}\right] \quad (10)$$

where γ is the Grüneisen parameter and scales as $\gamma(V) = \gamma_0\left(\frac{V}{V_0}\right)^q$, n is the number of atoms per formula unit, k is the Boltzmann constant, θ is the Debye temperature and varies as $\theta(V) = \theta_0 \exp\left[\frac{\gamma_0}{q}\left(1 - \left(\frac{V}{V_0}\right)^q\right)\right]$, and q is a unit-less scaling factor. Constraining q properly requires a large range of V/V_0. To aid this process we add an additional dataset comprising ambient pressure thermal expansion measurements by Touzelin (1978; via Massobrio and Meyer 1991). These measurements provide a strong constraint on q measurement while avoiding pressure calibration issues.

The entire high pressure, high temperature data set is fit to the above equations using a linear-least squares regression and fixing the values of V_0 to 77.4 Å^3 (Guo et al. 2002; Sumino et al. 1980) and θ_0=517.8 K (Freer 1981). Uncertainty in θ_0 has a relatively weak effect on the fitted parameters. Our best-fit parameters for the high P,T data set of Cobalt oxide are K_{0T}=190 (1) GPa, K′=3.49 (4), γ_0=1.54 (4), and q=2.87 (15) (Table 3; Figure 14a). Residuals between the

predicted pressure and measured pressure are mostly within one standard deviation one zero and show no significant trends with pressure or temperature (Figure 14b).

Notably we also attempted to fit an equation of state with regards to the NaCl pressure standard of Decker (1971) for the B1 phase and Fei et al. (2007) for the B2 phase. The pressure standard of Decker agreed well with that of Dorogokupets and Dewaele (2007). The equation of state of Fei et al. (2007), however, registered a systematically lower pressure than Dorogokupets and Dewaele that got as extreme as 4.5 GPa at the greatest compression. The effect of this was an apparent kink in the pressure volume curve of cobalt oxide. For this reason we disfavor the Fei pressure standard.

4. Discussion

Oxygen fugacity (fO_2) is one metric for comparing the free energy differences driving redox reactions. They can be used as a guide to the extent to which different species will oxidize or reduce one another at a given pressure and temperature. Following Campbell et al. (2009), for the oxidation reaction:

$$M + \frac{1}{2}O_2 = MO \tag{11}$$

the oxygen fugacity (fO_2) is a function of Gibbs free energy and temperature.

$$\ln fO_2 = \frac{2}{RT}\left(\Delta G_{MO} - \Delta G_M\right) \tag{12}$$

The pressure dependence of the fO_2 depends entirely on the Gibbs free energy, which varies with pressure as:

$$\Delta G(P,T) = \Delta G_{1bar}(T) + \int VdP \tag{13}$$

Gibbs free energies are well characterized at ambient pressure and high temperature (Chase 1998; Fredriksson 2004). We use Gibbs free energy values from the JANAF tables (Chase 1998). Evaluating the pressure term in equation 13 requires integrating along the appropriate isotherm for each component phase.

We use our newly constrained equation of state in conjunction with measurements on cobalt metal to extend the CoO/Co equilibria to high pressures and temperatures using Equations 12 and 13. Values used in this calculation are recorded in Table 3. The equation of state of cobalt metal is problematic. No simultaneous high pressure and temperature equation of state exists for cobalt metal. There are however independent measurements of: ambient temperature compressibility for the ε-hcp and β-fcc phases (Yoo et al. 2000), Debye temperature (Furukawa et al. 1982), and Grüneisen parameter from shockwave measurements (McQueen and Marsh 1960). The value of q is experimentally unconstrained, and is fixed at 1 in these calculations. When using this equation of state we must be cognizant that these measurements were performed independently, and may not work as a consistent whole. Furthermore, at pressures and temperatures relevant to the Earth, the γ-fcc phase of cobalt is the stable phase. Yoo et al. (2000) has argued that the β−fcc and γ−fcc phases are likely the same, however this assertion has not been verified experimentally. Acknowledging the uncertainty in the cobalt system, we compromise by calculating oxygen fugacity curves for both CoO/β-Co and for CoO/ε-Co.

We also recalculate the NiO/Ni and FeO/Fe equilibria using Campbell et al.'s (2009) data and method. Figure 15a shows the calculated CoO/Co fO_2 equilibria along a 2300 K isotherm. This isotherm is chosen to facilitate comparison with partitioning measurements (Li and Agee 1996; Kegler et al. 2008). Increasing pressure and temperature have opposite effects of the fO_2

equilibria. Increasing pressure tends to raise the fO_2 of each system, while increasing temperature lowers it.

Figure 15b shows the behavior of the CoO/Co and NiO/Ni equilibria relative to FeO/Fe to emphasize relative changes as a function of depth in the mantle. Oxides with high fO_2 buffers will tend to oxidize metals with lower fO_2 buffers. Nickel's fO_2 buffer rapidly decreases with pressure relative to iron's. This is in qualitative agreement with the rapid decrease in the metal-silicate partition coefficient of nickel with pressure (Li and Agee 1996; Kegler et al. 2008). Cobalt's behavior is more varied. The buffer between cobalt oxide and fcc β-Co has a positive trend, and the hcp ε-Co has a negative trend. Drawing analogy with the partitioning measurements, we would expect a negative trend shallower than nickel's. In this sense hcp agrees better. However the partitioning measurements also predict a crossing of nickel and cobalt's partition coefficients at ~30 GPa, in this sense fcc β-Co more closely matches our expectations. Our preferred explanation is that there are a number of issues at work making our measurements imperfectly correspond to trends in partition coefficients. First, it seems likely that the equation of state of fcc β-Co is a poor proxy significantly different from that of γ-Co and consequently a poor proxy. The positive trend in the fO_2 buffer is traceable primarily to the low V_0 of β-Co. The shallow Clapeyron slope between hcp ε-Co and γ-Co (Yoo et al. 2000) suggests that there is only a small volume change across the phase boundary. As such hcp-Co is probably a decent proxy for γ-Co at the conditions of interest. The CoO/Co_{hcp} buffer does not predict the same crossing between cobalt and nickel as do the partitioning measurements. This is likely attributable to some combination of non-unity activity coefficients and the partition experiments being between metal and silicate liquids as opposed to between metal and oxide solids.

Table 3. Equation of state parameters used in the calculation of oxygen fugacity buffers.

phase	V_0 (Å^3)	K (GPa)	K´	θ_0 (K)	γ_0	q	Source
B1 CoO	77.4 (fixed)	190 (1)	3.49 (4)	517.8 (fixed)	1.54 (4)	2.87 (15)	This study
B1 CoO	77.40	180	3.82				Guo et al. 2002
B1 CoO	77.26	186 (5) (K_S)					Sumino et al. 1980
Co (β-fcc)	6.223 (cc/mol)	224	5.8				Yoo et al. 2000
Co (ε-hcp)	6.624 (cc/mol)	199	3.6				Yoo et al. 2000
Co					1.97		McQueen and Marsh 1960
Co				445			Furukawa et al. 1982
NiO	10.973 (cc/mol)	190 (3)	5.4 (2)	480	1.80 (4)	1 (fixed)	Campbell et al. 2009
Ni	6.587 (cc/mol)	179 (3)	4.3 (2)	415	2.50 (6)	1 (fixed)	Campbell et al. 2009
FeO	12.256 (cc/mol)	146.9 (1.3)	4 (fixed)	380	1.42 (4)	1.3 (3)	Campbell et al. 2009
Fe (fcc)	7.076 (cc/mol)	133 (3)	5 (fixed)	470	1.95 (4)	1.6 (6)	Campbell et al. 2009
Fe (hcp)*	6.765 (cc/mol)	165	4.97	417	1.875	3.29	Dewaele 2006

*The equation of state of hcp iron incorporates additional terms not described here

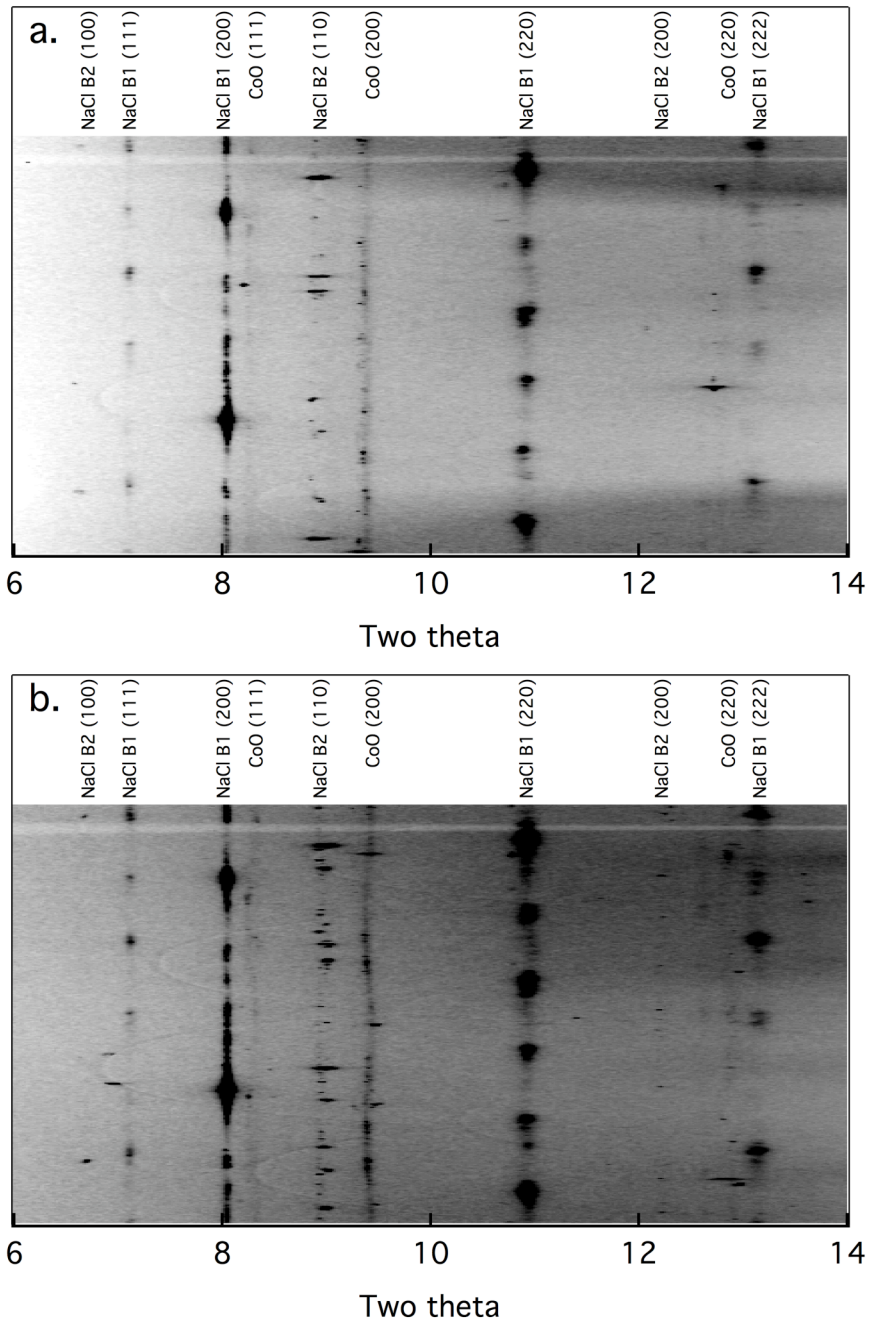

Figure 13. Representative caked diffraction patterns. **(a.)** Pattern obtained at 27 GPa at room temperature after laser heating. The cobalt oxide peaks show significant strain anisotropy. **(b.)** Pattern obtained at 30 GPa and ~2400 K. Strain anisotropy is not observed during heating.

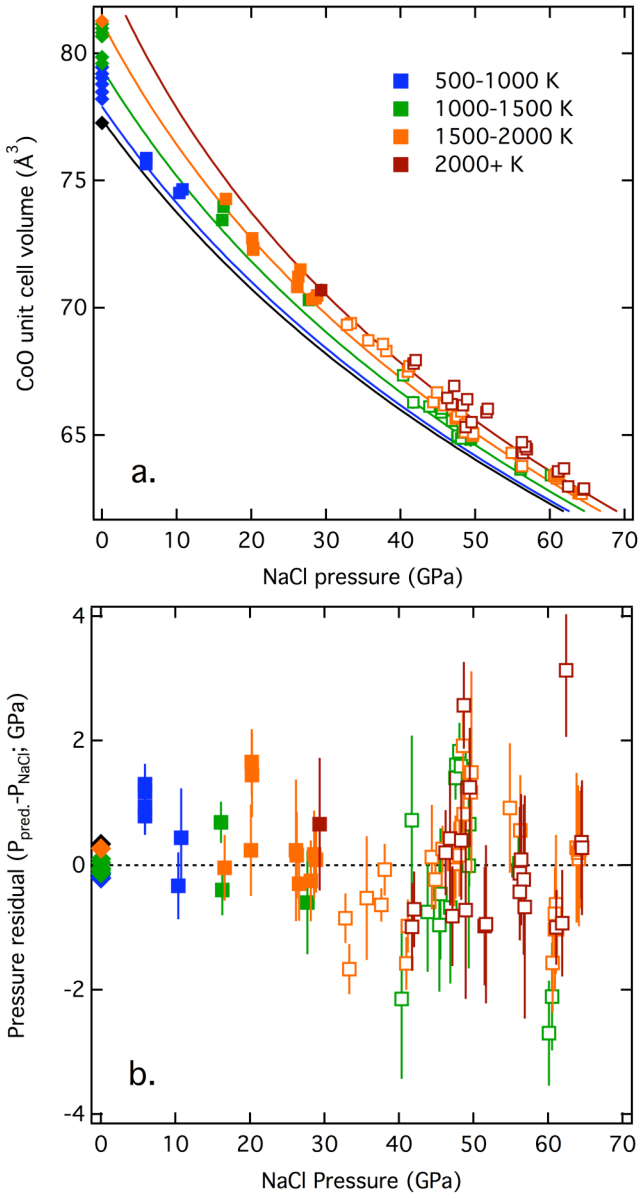

Figure 14. **(a.)** Measured cobalt oxide unit cell volume as a function of pressure and (binned) temperature. Filled squares: NaCl B1 pressure calibrant; Open squares: NaCl B2 pressure calibrant. Uncertainties are within the size of the symbols. Room pressure thermal expansion data from Touzelin 1978 are plotted as diamonds. Isotherms constructed from the best-fit thermoelastic properties and at the lower bound of each temperature bin are drawn. **(b.)** Pressure residuals from (a). Error bars show 1σ uncertainties.

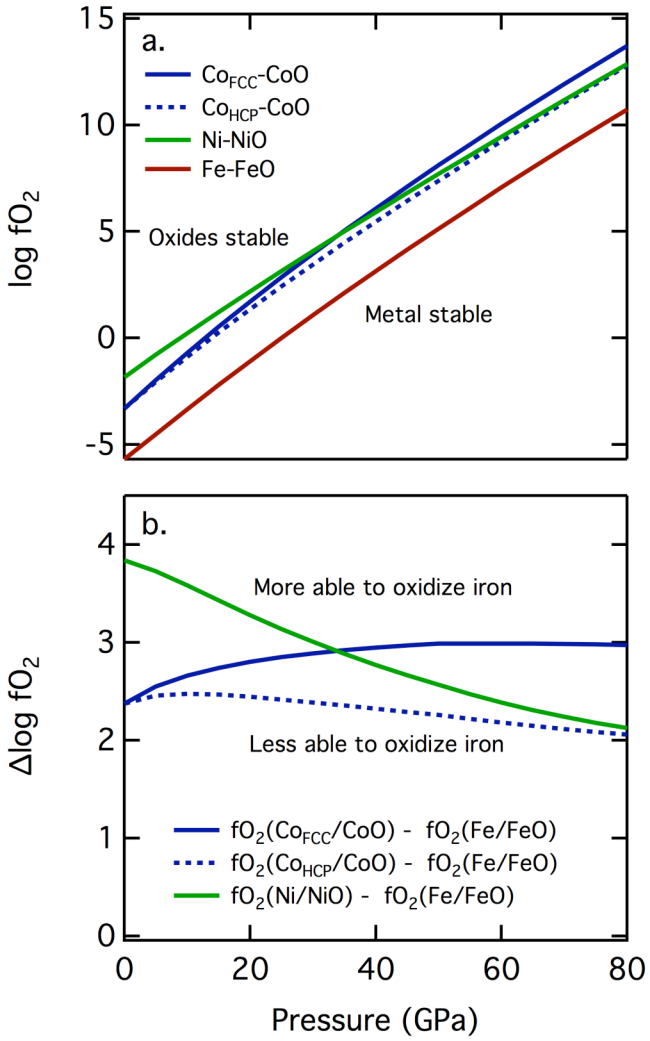

Figure 15. (a) Oxygen fugacity of C0oO/Co_{hcp}, CoO/Co_{fcc}, NiO/Ni, and FeO/Fe equilibria calculated up to 80 GPa at 2300 K using Equation 5. At 2300 K fcc cobalt is stable relative to hcp cobalt at all pressures. **(b)** fO_2 of CoO/Co_{hcp}, CoO/Co_{fcc} and NiO/Ni, relative to Fe/FeO. NiO/Ni and CoO/Co_{hcp} converge with iron with increasing pressure while CoO/Co_{fcc} diverge.

Conclusions

In each of the preceding chapters I have striven to bring each project to as satisfactory a conclusion as was possible given the constraints of the data. However, each would benefit from additional work. In the next several paragraphs I'd like to lay out future work that might further illuminate questions motivated, but only partially answered by this thesis.

The equation of state of osmium is interesting as an example of a very incompressible single element. In particular it exhibits a very high bulk modulus, Grüneisen parameter and q, particularly compared to the silicate and oxide measured elsewhere in this document. The first two parameters are directly related by the relation:

$$\gamma = \frac{\alpha K_T V}{C_V} \tag{14}$$

However, the thermodynamic requirements on q are less clear. It is commonly assumed that q should be unity, and γ/V constant with pressure, especially in shockwave experiments. This is not a requirement however, and at least some studies suggest that q may assume higher values and may also change with pressure. Constraining the systematics of this parameter would be well served both by more precise measurements of the equation of state and by measurements on a greater range of incompressible materials.

Measurements on the marginal effect of composition and temperature on the density and bulk sound velocity of ringwoodite are a valuable first step towards interpreting lateral heterogeneities in the transition zone. However, interpreting tomographic maps in terms of compositional and thermal anomalies requires additional knowledge. Ultimately, our understanding of lateral heterogeneity in the mantle is limited by the number of independent seismic observables. At best, we can independently measure V_s, V_p and ρ, making for a non-unique compositional and thermal interpretation. As a result we need to be judicious about the

parameters we use to interpret lateral variation. Further improvement could be achieved by testing the sensitivity of the seismic observables of ringwoodite to different compositional changes to confirm whether iron and temperature have the greatest predictive power relative to their expected variation in the transition zone. Repeating these tests on the equations of state of wadsleyite and majorite are another necessary step.

Understanding the relative redox behavior in the deep Earth has obvious implications for better understanding the conditions under which core-mantle separation occurred in the early Earth. Cobalt and nickel in particular have been valuable probes in constraining the pressure and temperature of the proto-core-mantle boundary. Our calculated CoO-Co oxygen fugacity buffer qualitatively agreed with some features of high pressure and temperature partitioning measurements. However, a more direct comparison could be made with several improvements. A single high pressure and temperature equation of state for γ-Co would be a good first step towards the calculation of the appropriate buffer at high temperatures. Measuring the equation of state of cobalt and nickel silicates (as opposed to oxides) would also allow for a more direct comparison with partitioning measurements in the upper mantle pressure regime.

Appendix A: Tabled data

Table A1. Complete set of data used in the osmium study. It should be noted that temperatures reported are the average sample temperatures and 7% lower than the measured temperatures.

ALSOS3	Os V ($Å^3$)	sd	c/a	sd	NaCl V ($Å^3$)	sd	P (GPa)	sd	T (K)	sd
	27.422	0.000	1.5817	0.0000	144.860	0.445	8.65	0.01	300	5
	27.448	0.001	1.5823	0.0001	145.036	0.425	8.58	0.01	300	5
	27.420	0.016	1.5817	0.0008	145.732	0.166	8.28	0.00	300	5
	27.433	0.018	1.5807	0.0009	145.442	0.162	8.40	0.00	300	5
	27.455	0.003	1.5829	0.0001	144.400	0.202	8.85	0.00	300	5
	27.436	0.008	1.5819	0.0004	144.937	0.386	8.62	0.01	300	5
	27.262	0.042	1.5827	0.0021	139.406	0.244	11.28	0.01	300	5
	27.364	0.006	1.5815	0.0003	141.051	0.390	10.43	0.01	300	5
	27.048	0.026	1.5836	0.0013	133.575	0.326	14.75	0.01	300	5
	27.060	0.007	1.5817	0.0003	133.077	0.028	15.08	0.00	300	5
	27.112	0.005	1.5807	0.0002	135.560	0.152	13.48	0.01	300	5
					transition to B2 phase					
	26.220	0.013	1.5849	0.0007	27.513	0.070	29.68	0.03	300	5
	26.260	0.021	1.5862	0.0010	27.264	0.073	30.88	0.03	300	5
	26.154	0.013	1.5818	0.0007	27.571	0.004	29.41	0.00	300	5
	26.228	0.011	1.5855	0.0005	27.630	0.017	29.14	0.01	300	5
	26.245	0.032	1.5868	0.0016	27.506	0.031	29.71	0.01	300	5
	25.870	0.018	1.5867	0.0009	26.177	0.007	36.95	0.00	300	5
	26.134	0.002	1.5864	0.0001	27.124	0.007	31.58	0.00	300	5
	25.470	0.012	1.5833	0.0006	25.195	0.102	43.82	0.06	300	5
	25.646	0.003	1.5878	0.0001	25.274	0.010	43.21	0.01	300	5
	25.559	0.001	1.5846	0.0001	25.247	0.022	43.42	0.01	300	5
	25.536	0.019	1.5853	0.0010	25.201	0.014	43.77	0.01	300	5

	25.329	0.005	1.5849	0.0003	24.813	0.007	46.92	0.00	300	5
	25.401	0.052	1.5844	0.0027	24.695	0.003	47.94	0.00	300	5
	25.314	0.016	1.5846	0.0008	24.356	0.014	51.02	0.01	300	5
	25.260	0.007	1.5851	0.0004	24.442	0.039	50.22	0.03	300	5
	25.250	0.084	1.5851	0.0044	24.385	0.010	50.75	0.01	300	5
	25.285	0.019	1.5849	0.0010	24.326	0.021	51.30	0.01	300	5
ALSOS8	Os V ($Å^3$)	sd	c/a	sd	NaCl V ($Å^3$)	sd	P (GPa)	sd	T (K)	sd
	27.802	0.007	1.5807	0.0003	162.889	0.032	2.74	0.01	300	5
	27.796	0.012	1.5806	0.0006	162.843	0.074	2.75	0.02	300	5
	27.616	0.017	1.5805	0.0008	152.862	0.126	5.48	0.04	300	5
	27.521	0.024	1.5809	0.0011	146.258	0.075	7.88	0.03	300	5
	27.490	0.012	1.5817	0.0006	147.059	0.167	7.56	0.07	300	5
	27.498	0.028	1.5844	0.0013	148.424	0.202	7.03	0.08	300	5
	27.971	0.076	1.5881	0.0035	147.143	0.273	10.23	0.08	2433	427
	28.161	0.244	1.5919	0.0109	148.191	0.222	15.51	0.1	2234	81
	28.332	0.238	1.5929	0.0110	150.501	0.112	9.16	0.04	2107	74
	28.413	0.447	1.5856	0.0197	149.696	0.139	9.77	0.05	2300	93
	28.536	0.317	1.5908	0.0140	149.334	0.177	10.14	0.07	2451	96
	28.556	0.164	1.5979	0.0075	149.111	0.088	10.35	0.03	2528	113
	28.114	0.268	1.5855	0.0120	147.970	0.290	9.74	0.11	1880	-
	27.326	0.109	1.5816	0.0052	137.547	0.568	12.08	0.32	300	5
	27.152	0.053	1.5832	0.0025	134.798	0.109	13.71	0.07	300	5
	27.607	0.051	1.5878	0.0024	136.571	0.281	15.39	0.16	1965	82
	27.919	0.253	1.5831	0.0117	138.156	0.401	15.06	0.22	2313	106
	28.080	0.112	1.5893	0.0052	139.830	0.409	14.85	0.21	2740	193
	28.169	0.426	1.5757	0.0194	141.057	0.275	13.73	0.14	2441	90
	28.345	0.477	1.5726	0.0216	141.353	0.123	14.23	0.07	2842	415
	28.582	0.049	1.5951	0.0022	147.784	0.033	10.82	0.01	2501	42
	27.364	0.068	1.5799	0.0032	142.301	0.255	9.62	0.12	300	5

	26.892	0.130	1.5830	0.0063	129.285	0.080	17.53	0.06	300	5
	27.487	0.071	1.5891	0.0034	134.645	0.462	16.69	0.29	2022	105
	27.700	0.037	1.5860	0.0017	138.230	0.101	17.14	0.06	2675	69
	27.486	0.012	1.5819	0.0005	143.535	0.115	9.05	0.05	300	5
	27.662	0.040	1.5854	0.0019	139.699	0.062	13.69	0.03	1994	-
	28.133	0.122	1.5808	0.0056	152.562	1.923	9.00	0.61	2447	511
	27.931	0.113	1.5807	0.0052	152.317	0.497	9.48	0.17	2693	487
	27.649	0.074	1.5809	0.0035	149.247	0.558	6.72	0.20	300	5
HPCATOS3	Os V ($Å^3$)	sd	c/a	sd	MgO V ($Å^3$)	sd	P (GPa)	sd	T (K)	sd
	27.481	0.011	1.5805	0.0005	71.993	0.008	6.42	0.02	300	5
	27.575	0.032	1.5830	0.0014	71.948	0.000	10.90	0.01	1756	7
	27.693	0.036	1.5792	0.0016	72.725	0.010	8.45	0.03	1598	6
	27.841	0.004	1.5870	0.0002	73.101	0.003	8.16	0.02	1792	30
	27.791	0.039	1.5889	0.0018	73.180	0.036	8.23	0.09	1872	5
	27.930	0.006	1.5919	0.0003	72.904	0.003	8.53	0.07	1759	91
	27.430	0.008	1.5815	0.0004	71.413	0.006	7.96	0.02	300	5
	27.421	0.003	1.5819	0.0001	71.464	0.009	7.82	0.03	300	5
	27.315	0.171	1.5853	0.0079	70.257	0.008	11.21	0.02	300	5
	27.243	0.050	1.5850	0.0023	70.228	0.000	11.30	0.00	300	5
	27.173	0.016	1.5830	0.0007	69.846	0.006	15.32	0.07	1299	78
	27.252	0.032	1.5823	0.0015	69.747	0.003	16.04	0.04	1433	43
	27.378	0.080	1.5846	0.0037	70.060	0.010	15.7	0.06	1626	76
	27.501	0.185	1.5888	0.0084	69.962	0.005	17.2	0.14	2009	213
	27.366	0.156	1.5936	0.0072	69.741	0.002	18.39	0.03	2174	45
	27.429	0.186	1.5942	0.0086	69.932	0.011	18.97	0.07	2536	117
	27.627	0.275	1.5924	0.0124	69.771	0.009	20.19	0.08	2769	150
	27.114	0.038	1.5830	0.0018	68.920	0.007	15.32	0.02	300	5
	27.089	0.031	1.5831	0.0014	68.934	0.005	15.28	0.02	300	5
	26.943	0.020	1.5837	0.0009	71.993	0.008	17.08	0.01	300	5

	26.952	0.020	1.5836	0.0009	72.998	0.014	17.17	0.01	300	5
	26.954	0.031	1.5822	0.0014	71.948	0.000	21.84	0.03	1318	25
	27.014	0.031	1.5823	0.0014	72.725	0.010	22.28	0.04	1543	47
	27.051	0.069	1.5844	0.0032	73.101	0.003	22.95	0.05	1796	62
	27.273	0.099	1.5819	0.0045	73.180	0.036	24.05	0.03	2221	40
	27.396	0.101	1.5794	0.0046	72.904	0.003	23.72	0.04	2228	64
	27.583	0.220	1.5799	0.0098	71.413	0.006	23.1	0.1	2256	161
	27.022	0.018	1.5755	0.0008	71.464	0.009	20.37	0.03	300	5
	27.002	0.023	1.5757	0.0011	72.039	0.011	20.42	0.01	300	5
	26.887	0.045	1.5796	0.0023	71.993	0.008	20.80	0.01	300	5
	26.877	0.050	1.5795	0.0026	72.998	0.014	20.67	0.02	300	5
	26.760	0.019	1.5843	0.0010	71.948	0.000	25.09	0.06	1270	59
	26.732	0.021	1.5846	0.0010	72.725	0.010	26.27	0.07	1459	93
	26.768	0.033	1.5830	0.0015	73.101	0.003	26.97	0.16	1674	214
	26.986	0.023	1.5900	0.0012	73.180	0.036	27.2	0.15	1832	218
	26.835	0.039	1.5809	0.0018	72.904	0.003	27.54	0.02	1961	32
	26.764	0.057	1.5866	0.0027	71.413	0.006	29.42	0.16	2336	270
	26.625	0.056	1.5832	0.0026	71.464	0.009	24.11	0.01	300	5
	26.623	0.052	1.5829	0.0024	72.039	0.011	24.11	0.01	300	5
	26.486	0.044	1.5816	0.0021	71.993	0.008	26.41	0.01	300	5
	26.508	0.052	1.5837	0.0025	72.998	0.014	26.47	0.01	300	5
	26.406	0.031	1.5845	0.0015	71.948	0.000	32.32	0.12	1742	161
	26.404	0.023	1.5844	0.0012	72.725	0.010	34.46	0.11	2144	180
	26.400	0.023	1.5846	0.0011	73.101	0.003	34.66	0.17	2137	271
	26.417	0.021	1.5891	0.0010	73.180	0.036	35.01	0.04	2108	52
	26.425	0.040	1.5926	0.0021	72.904	0.003	37.05	0.28	2432	485
	26.176	0.010	1.5878	0.0005	71.413	0.006	33.59	0.01	300	5
	26.169	0.008	1.5875	0.0004	71.464	0.009	33.78	0.01	300	5
	25.805	0.022	1.5868	0.0012	71.993	0.008	39.34	0.02	300	5
	25.823	0.018	1.5883	0.0009	72.998	0.014	39.40	0.01	300	5
	25.809	0.020	1.5871	0.0010	71.948	0.000	39.38	0.01	300	5
	25.927	0.009	1.5876	0.0005	72.725	0.010	42.6	0.14	1270	168

	25.986	0.012	1.5907	0.0006	73.101	0.003	42.99	0.19	1468	241
	25.933	0.028	1.5920	0.0014	73.180	0.036	43.8	0.07	1680	100
	25.898	0.034	1.5926	0.0017	72.904	0.003	44.67	0.12	1839	180
	25.932	0.023	1.5954	0.0011	71.413	0.006	45.69	0.16	1781	229
	25.873	0.058	1.5918	0.0028	71.464	0.009	47.1	0.04	2016	18
GSECARSOS4	Os V ($Å^3$)	sd	c/a	sd	MgO V ($Å^3$)	sd	P (GPa)	sd	T (K)	sd
	26.733	0.007	1.5893	0.0003	67.148	0.006	24.98	0.34	1533.5	418.171
	26.899	0.012	1.5896	0.0006	67.327	0.006	25.09	0.30	1775.5	406.068
	26.398	0.007	1.5857	0.0003	65.909	0.005	26.14	0.02	300	5
	26.390	0.005	1.5858	0.0003	65.854	0.007	26.36	0.03	300	5
	26.170	0.012	1.5832	0.0006	64.387	0.015	32.57	0.07	300	5
	26.028	0.007	1.5844	0.0003	63.848	0.026	35.03	0.80	300	5
	26.042	0.008	1.5835	0.0004	63.885	0.020	34.85	0.20	300	5
	26.111	0.012	1.5823	0.0006	64.246	0.008	33.20	0.04	300	5
	26.109	0.009	1.5840	0.0005	64.285	0.016	33.03	0.22	300	5
	26.038	0.022	1.5864	0.0011	64.745	0.003	30.99	0.01	300	5
	26.076	0.068	1.5851	0.0031	65.011	0.005	33.43	0.16	1543	207
	26.297	0.149	1.5788	0.0068	65.466	0.011	31.90	0.64	1663	395
	26.248	0.149	1.5795	0.0068	65.312	0.023	32.58	2.18	1676	463
	26.125	0.003	1.5853	0.0002	64.740	0.020	31.02	0.53	300	5
	26.156	0.023	1.5830	0.0012	64.764	0.036	30.91	0.69	300	5
	25.899	0.013	1.5836	0.0007	63.839	0.016	35.07	0.07	300	5
	25.852	0.008	1.5843	0.0004	63.319	0.016	37.53	0.81	300	5
	25.809	0.009	1.5843	0.0005	62.719	0.021	40.50	0.15	300	5
	25.992	0.009	1.5870	0.0005	63.073	0.014	42.15	0.24	1491	287
	25.915	0.006	1.5858	0.0003	62.220	0.102	43.06	0.53	300	5
	25.906	0.016	1.5860	0.0008	62.435	0.169	41.94	0.87	300	5
	25.885	0.005	1.5883	0.0003	61.758	0.085	48.75	0.48	1428	138
	25.879	0.016	1.5872	0.0009	62.251	0.061	46.06	0.34	1408	151

	25.901	0.007	1.5892	0.0003	61.694	0.053	49.07	0.35	1417	245
	25.924	0.002	1.5888	0.0001	62.036	0.355	47.63	1.90	1550	308
	25.992	0.009	1.5880	0.0005	61.876	0.443	48.86	2.40	1672	366
	26.100	0.016	1.5920	0.0009	61.757	0.017	49.96	0.36	1822	485
	26.159	0.007	1.5908	0.0004	62.052	0.306	49.14	1.65	2067	434
	25.836	0.009	1.5840	0.0005	61.645	0.047	46.14	0.26	300	5
	25.822	0.013	1.5837	0.0007	61.595	0.017	46.42	0.09	300	5
	25.654	0.018	1.5883	0.0009	61.608	0.036	46.34	0.20	300	5
	25.672	0.011	1.5881	0.0006	61.800	0.050	45.30	0.27	300	5
	Os V ($Å^3$)	sd	c/a	sd	MgO V ($Å^3$)	sd	P (GPa)	sd	T (K)	sd

Table A2. Data used in the ringwoodite study.

File	NaCl B1 lattice parameter (Å)	Ringwoodite lattice parameter (Å)	Upstream temperature (K)[3]	Downstream temperature (K)[3]	Density (cm^3/mol)	NaCl Pressure (GPa)
Fay008heat	5.2319 (149)	8.1573[1] (30)	300	1292	43.22 (3)	9.35 (44)
Fay009heat	5.2405 (66)	8.1565 (40)	1124	1172	43.24 (4)	9.77 (30)
Fay010heat	5.2456 (38)	8.1629 (46)	1188	1251	43.13 (4)	9.75 (23)
Fay011heat	5.2465 (32)	8.1596 (33)	1234	1284	43.19 (3)	9.81 (25)
Fay012heat	5.2501 (30)	8.1655 (57)	1342	1363	43.09 (5)	9.91 (26)
Fay013heat	5.2503 (30)	8.1697 (49)	1522	1500	43.03 (4)	9.85 (24)
Fay014quench	5.2560 (28)	8.1279[2] (252)	300	300	43.69 (23)	8.62 (21)
Fay019preheat	5.2023 (28)	8.0921[2] (1028)	300	300	44.28 (97)	10.60 (13)
Fay020heat	5.2315 (96)	8.1567 (37)	1417	1378	43.23 (3)	10.48 (59)
Fay021heat	5.2361 (73)	8.1668 (43)	1886	1858	43.07 (4)	10.80 (39)
Fay022heat	5.2372 (81)	8.1680 (36)	1947	1902	43.05 (3)	10.82 (28)
Fay023heat	5.2408 (96)	8.1687 (22)	1683	1648	43.04 (2)	10.36 (33)
Fay024heat	5.2410 (98)	8.1678 (24)	1698	1672	43.06 (2)	10.40 (32)
Fay025heat	5.2439 (96)	8.1751 (23)	2806	2224	42.94 (2)	11.48 (54)
Fay026heat	5.2502 (54)	8.1771 (19)	1940	2000	42.91 (2)	10.70 (67)
Fay027heat	5.2455 (93)	8.1759 (24)	1806	2000	42.93 (2)	10.61 (82)
Fay028heat	5.2424 (50)	8.1744 (25)	2209	2254	42.95 (2)	11.13 (49)
Fay029quench	5.1947 (132)	8.0785[2] (348)	300	300	44.50 (33)	10.94 (13)

1) Value excluded from fitting due to large temperature gradient.

2) Value excluded from fitting due to presence of large deviatoric stress.

3) The temperature of NaCl was assumed to be at the midpoint between the measured temperature of the ringwoodite and 300 K as in Seagle *et al.* [*2008*].

Table A3. Data used in the cobalt oxide study. Measured unit cell volumes for sample and standard, average measured temperatures, and inferred pressures from the NaCl standard. NaCl unit cell volumes are the B2 structure unless otherwise indicated (* =B1)

.

file	NaCl Volume (Å^3)	Uncertainty (Å^3)	NaCl P (GPa)	Uncertainty (GPa)	CoO V (Å^3)	Uncertainty (Å^3)	Sample Temperature (K)	Uncertainty (K)
DAC_I_060*	154.633	0.220	5.91	0.07	75.887	0.042	832	7
DAC_I_061*	154.288	0.266	5.91	0.10	75.862	0.049	759	37
DAC_I_062*	154.223	0.517	5.92	0.18	75.652	0.048	754	39
DAC_I_063*	154.031	0.443	5.90	0.14	75.659	0.150	695	16
DAC_I_067*	142.355	0.276	10.36	0.16	74.510	0.114	700	64
DAC_I_068*	142.355	0.291	10.76	0.23	74.657	0.087	963	118
DAC_I_080*	133.487	0.287	16.12	0.20	73.445	0.029	1321	42
DAC_I_081*	133.622	0.528	16.58	0.36	74.281	0.020	1672	63
DAC_I_082*	133.480	0.476	16.27	0.32	73.968	0.021	1416	40
DAC_I_093*	128.158	0.357	20.26	0.30	72.358	0.142	1597	59
DAC_I_094*	128.190	0.408	20.21	0.33	72.279	0.086	1581	48
DAC_I_097*	128.264	0.447	20.12	0.37	72.728	0.139	1560	72
DAC_I_103*	121.224	0.347	26.15	0.47	70.817	0.052	1534	183
DAC_I_105*	121.513	0.400	26.28	0.42	71.215	0.105	1783	70
DAC_I_106*	121.450	0.335	26.57	0.36	71.502	0.078	1920	67
DAC_I_113*	119.355	0.394	27.71	0.46	70.305	0.109	1340	99
DAC_I_114*	119.188	0.436	28.17	0.48	70.341	0.095	1510	40
DAC_I_115*	119.050	0.323	28.62	0.36	70.374	0.141	1692	41
DAC_I_116*	118.998	0.289	28.84	0.32	70.490	0.102	1791	20
DAC_I_117*	119.023	0.179	29.35	0.22	70.693	0.256	2111	53

DAC_I_123	27.825	0.002	33.31	0.04	69.395	0.090	1562	22
DAC_I_124	27.927	0.028	32.79	0.16	69.340	0.081	1578	22
DAC_I_133	27.464	0.008	35.67	0.20	68.724	0.181	1738	105
DAC_I_143	27.212	0.010	37.63	0.10	68.580	0.033	1983	38
DAC_I_144	27.136	0.026	38.06	0.19	68.302	0.058	1965	49
DAC_I_154	26.556	0.039	40.35	0.28	67.348	0.258	1234	21
DAC_I_155	26.569	0.035	40.97	0.27	67.495	0.041	1595	52
DAC_I_156	26.635	0.033	41.18	0.25	67.710	0.044	1930	54
DAC_I_157	26.608	0.038	41.73	0.28	67.815	0.128	2121	48
DAC_I_158	26.627	0.038	42.01	0.29	67.944	0.097	2329	56
DAC_I_162	26.328	0.025	41.69	0.18	66.289	0.260	1127	1
DAC_I_171	26.018	0.029	43.84	0.23	66.121	0.175	1108	34
DAC_I_172	26.071	0.027	44.38	0.21	66.302	0.155	1569	21
DAC_I_173	26.104	0.024	44.87	0.20	66.679	0.075	1938	42
DAC_I_183	25.819	0.042	45.42	0.33	65.884	0.191	1159	6
DAC_I_184	25.878	0.034	45.54	0.28	66.042	0.188	1441	47
DAC_I_185	25.928	0.034	45.84	0.27	66.178	0.040	1780	29
DAC_I_186	25.960	0.025	46.26	0.21	66.460	0.122	2112	38
DAC_I_189	25.945	0.028	47.15	0.24	66.935	0.143	2500	57
DAC_I_193	25.635	0.050	46.89	0.41	65.556	0.212	1197	10
DAC_I_194	25.661	0.046	47.39	0.38	65.651	0.099	1542	36
DAC_I_195	25.672	0.055	47.59	0.46	65.732	0.078	1686	51
DAC_I_196	25.685	0.052	48.11	0.46	65.933	0.042	1994	88
DAC_I_197	25.868	0.003	46.83	0.18	66.214	0.185	2050	89
DAC_I_198	25.690	0.060	48.92	0.53	66.407	0.239	2417	99
DAC_I_199	25.738	0.073	48.34	0.60	66.174	0.127	2314	67
DAC_I_207	25.497	0.032	48.11	0.30	64.867	0.031	1265	65
DAC_I_208	25.525	0.034	47.58	0.29	64.914	0.016	1110	35
DAC_I_209	25.546	0.031	47.67	0.26	64.973	0.036	1238	17
DAC_I_210	25.533	0.046	48.30	0.39	65.098	0.025	1498	33

DAC_I_211	25.535	0.052	48.60	0.44	65.120	0.050	1656	11
DAC_I_212	25.547	0.050	48.67	0.42	65.413	0.110	1736	32
DAC_I_213	25.615	0.070	48.69	0.59	65.317	0.048	2012	56
DAC_I_214	25.534	0.058	49.49	0.50	65.507	0.140	2093	59
DAC_I_223	25.299	0.040	49.36	0.35	64.827	0.283	1096	4
DAC_I_224	25.347	0.043	49.43	0.37	64.891	0.164	1323	7
DAC_I_225	25.382	0.058	49.64	0.50	64.975	0.064	1565	39
DAC_I_226	25.417	0.047	49.72	0.40	65.064	0.279	1743	24
DAC_I_229	25.368	0.047	51.50	0.40	65.900	0.162	2424	3
DAC_I_230	25.386	0.055	51.67	0.48	66.026	0.216	2583	57
DAC_I_238	24.552	0.039	56.04	0.39	63.648	0.081	1181	4
DAC_I_240	24.578	0.041	56.13	0.40	63.743	0.056	1342	11
DAC_I_242	24.605	0.037	56.28	0.37	63.778	0.129	1530	41
DAC_I_244	24.709	0.053	56.38	0.51	64.291	0.155	2038	18
DAC_I_245	24.721	0.061	56.21	0.59	64.340	0.142	2005	62
DAC_I_248	24.681	0.072	56.88	0.70	64.448	0.278	2153	48
DAC_I_249	24.801	0.012	56.22	0.14	64.724	0.129	2358	39
DAC_I_250	24.738	0.004	56.71	0.05	64.549	0.206	2321	18
DAC_I_252	24.847	0.081	54.88	0.79	64.305	0.080	1908	107
DAC_I_261	24.136	0.051	60.13	0.53	63.420	0.103	1228	21
DAC_I_262	24.143	0.050	60.55	0.53	63.425	0.105	1461	37
DAC_I_263	24.160	0.038	60.60	0.40	63.399	0.108	1559	24
DAC_I_264	24.199	0.045	60.91	0.47	63.469	0.070	1888	22
DAC_I_265	24.193	0.047	61.20	0.50	63.553	0.059	1999	28
DAC_I_266	24.207	0.047	61.08	0.49	63.577	0.057	2006	1
DAC_I_267	24.196	0.045	61.88	0.47	63.693	0.111	2333	46
DAC_I_269	24.177	0.042	61.06	0.44	63.389	0.163	1859	6
DAC_I_270	24.142	0.041	60.93	0.43	63.299	0.141	1629	17
DAC_I_281	23.900	0.052	63.83	0.57	62.713	0.159	1837	37
DAC_I_282	23.894	0.052	64.02	0.59	62.738	0.131	1893	65

DAC_I_283	23.873	0.058	64.26	0.64	62.697	0.101	1908	39
DAC_I_284	23.883	0.056	64.12	0.62	62.737	0.134	1891	27
DAC_I_285	23.911	0.055	64.49	0.62	62.862	0.090	2197	61
DAC_I_286	23.913	0.064	64.55	0.71	62.898	0.122	2234	44
DAC_I_287	24.176	0.037	62.42	0.48	62.978	0.119	2494	128
Touzelin (1978)	-	-	-	-	77.260	0.014	299	5
Touzelin (1978)	-	-	-	-	78.205	0.014	589	5
Touzelin (1978)	-	-	-	-	78.480	0.014	683	5
Touzelin (1978)	-	-	-	-	78.788	0.014	774	5
Touzelin (1978)	-	-	-	-	79.036	0.014	852	5
Touzelin (1978)	-	-	-	-	79.202	0.014	911	5
Touzelin (1978)	-	-	-	-	79.457	0.014	980	5
Touzelin (1978)	-	-	-	-	79.596	0.014	1039	5
Touzelin (1978)	-	-	-	-	79.851	0.014	1117	5
Touzelin (1978)	-	-	-	-	80.672	0.014	1326	5
Touzelin (1978)	-	-	-	-	80.818	0.014	1375	5
Touzelin (1978)	-	-	-	-	80.980	0.014	1427	5
Touzelin (1978)	-	-	-	-	81.149	0.014	1476	5
Touzelin	-	-	-	-	81.262	0.014	1527	5

(1978)								

References

F. Birch, Phys. Rev. **71**, 809 (1947).

J. M. Brown and T. J. Shankland, Geophys. J. R. Astr. Soc., **66**, 579 (1981)

J. M. Brown, J. App. Phys., **86**, 5801 (1999)

W. A. Caldwell, M. Kunz, R. S. Celestre, E. E. Domning, M. J. Walter, D. Walker, J. Glossinger, A. A. MacDowell, H. A. Padmore, R. Jeanloz, and S. M. Clark, Nuc. Instrum. Met. Phys. Res. Sec. A. **582**, 221 (2007).

A. J. Campbell, L. Danielson, K. Righter, C. T. Seagle, Y. B. Wang, and V. B. Prakapenka, Earth Pl. Sci. Lett., 286, 556 (2009)

A. J. Campbell, C. T. Seagle, D. L. Heinz, G. Y. Shen, and V. B. Prakapenka, Phys. Earth Pl. Int. **162**, 119 (2007).

M.W. Chase Jr., NIST-JANAF Thermochemical Tables, 4th ed. : J. Phys. Chem. Ref. Data Monograph No. 9. American Institute of Physics (1998).

H. Y. Chung, M. B. Weinberger, J. B. Levine, A. Kavner, J. M. Yang, S. H. Tolbert, and R. B. Kaner, Science **316**, 436 (2007).

R. W. Cumberland, M. B. Weinberger, J. J. Gilman, S. M. Clark, S. H. Tolbert, and R. B. Kaner, J. Am. Chem. Soc. **127**, 7264 (2005).

H. Cynn, J. E. Klepeis, C. S. Yoo, and D. A. Young, Phys. Rev. Lett. **88**, 135701 (2002).

D. L. Decker, J. App. Phys., **42**, 3239 (1971).

A. Dewaele, P. Loubeyre, F. Occelli, , M Mezouar, P. I. Dorogokupets, and M. Torrent, Phys. Rev. Lett., **97**, 215504 (2006).

A. Dewaele, G. Fiquet, and P. Gillet, Rev. Sci. Instrum. **69**, 2421 (1998).

P. I. Dorogokupets and A. Dewaele, Int. J. High Pres. Res., **27**, 431 (2007).

T. S. Duffy and Y. B. Wang, in Ultrahigh-Pressure Mineralogy, edited by R.J. Hemley [Rev. Min, 37, 425-457] (1998).

Y. Fei, A. Ricolleau, M. Frank, K. Mibe, G. Shen, and V. Prakapenka, Proc. Natl. Acad. Sci., **104**, 9182 (2007)

P. Fredriksson and S. Seetharaman, Scandinavian J. Mett., 33, 305 (2004)

R. Freer, J. Mat. Sci., **16**, 3225 (1981).

G. T. Furukawa, T. B. Douglas and N. Pearlman, N., Heat Capacities, in: Zemansky, M. W., Gray, D. E. (Eds.), American Institute of Physics Handbook: Third Edition. McGraw-Hill., New York, pp. 4-115 (1982).

C. M. S. Gannarelli, D. Alfe, and M. J. Gillan, Phys. Earth Pl. Int. **152**, 67 (2005)

Q. Guo, H. K. Mao, J. Hu, J. Shu, and R. J. Hemley (2002), J. Phys.: Condens. Matter, **14**, 11369 (2002).

A. P. Hammersley, S. O. Svensson, M. Hanfland, A. N. Fitch, and D. Hausermann, H. Pres. Res., 14(4-6), 235 (1996).

R. M. Hazen, Science, **259**, 206 (1993).

M. Hebbache, L. Stuparevic, and D. Zivkoric, Solid state comm. **139**, 227 (2006).

K. Hirose, Rev. Geophys., **44**, RG3001 (2006).

I. Jackson and S. M. Rigden, Phys. Earth Pl. Int. **96**, 85 (1996).

R.B. Kaner, J. J. Gilman, and S. H. Tolbert, Science **308**, 1268 (2005).

A. Kavner and T. S. Duffy, J. App. Phys. **89**, 1907 (2001).

A. Kavner and W. R. Panero, Phys. Earth Pl. Int. **143**, 527 (2004).

P. Kegler, A. Holzheid, D. J. Frost, D. C. Rubie, R. Dohmen, and H. Palme, Earth Pl. Sci. Lett., **268**, 28 (2008).

T. Kenichi, Phys. Rev. B **70**, 012101 (2004).

B. Kiefer and T. S. Duffy, J. App. Phys. **97**, 114902 (2005).

O. L. Kuskov, Geokhimiya, **8**, 1119 (1984).

J. M. Leger and J. Haines, Endeavour **21**, 121 (1997).

J. Li and C. B. Agee, Geochimica et Cosmochimica Acta, **65**, 1821 (2001).

J. Li and C. B. Agee, Nature, **381**, 686 (1996).

Q. Liu, W. Liu, M. L. Whitaker, L. P. Wang, and B. S. Li, H. Pres. Res., **28**, 405 (2008).

Y. Ma, M. Somayazulu, G. Shen, H. K. Mao, J. Shu, and R. J. Hemley, Phys. Earth Pl. Int. **143**, 455 (2004).

C. Massobrio and M. Meyer, J. Phys.: Condens. Matter, **3**, 279 (1991).

H. K. Mao, T. Takahash, W. A. Bassett, and J. S. Weaver, J. Geophys. Res., **74**, 1061 (1969).

G. Masters and D. Gubbins, Phys. Earth Pl. Int. **140**, 159 (2003).

M. Matsui, E. Ito, T. Katsura, D. Yamazaki, T. Yoshino, A. Yokoyama, and K. Funakoshi, J. App. Phys. **105**, 013505 (2009).

R. G. McQueen and S. P. Marsh, J. App. Phys., **31**, 1253 (1960).

Y. Meng, G. Shen, and H. K. Mao, J. Phys. Condensed Matter. **18**, S1097 (2006).

Y. Meng, Y. Fei, D. J. Weidner, G. D. Gwanmesia, and J. Hu, Phys. Chem. Min., **21**, 407 (1994).

Y. Meng and D. J. Weidner, Geophys. Res. Lett. **20**, 1147 (1993).

P. Modak, A. K. Verma, R. S. Rao, B. K. Godwal, L. Stixrude, and R. Jeanloz, J. Phys. Condens. Matter **19**, 016208 (2007)

M. Murakami, K. Hirose, S. Ono, T. Tsuchiya, M. Isshiki, and T. Watanuki, Phys. Earth. Pl. Int., **146**, 273 (2004)

F. Nestola, T. B. Ballaran, M. Koch-Muller, T. Balic-Zunic, M. Taran, L. Olsen, F. Princivalle, L. Secco, and L. Lundegaard, Phys. Earth Pl. Int., **183**, 421 (2010).

Y. Nishihara, E. Takahashi, K. N. Matsukage, T. Iguchi, K. Nakayama, and K. Funakoshi, Phys. Earth Pl. Int., **143**, 33 (2004)

H. St. C. O'Neill, D. Canil, and D. C. Rubie, J. Geophys. Res., **103**, 12239 (1998).

F. Occelli, D. L. Farber, J. Badro, C. M. Aracne, D. M. Teter, M. Hanfland, B. Canny, and B. Couzinet, Phys. Rev. Lett. **93**, 095502 (2004).

C. Pantea, I. Mihut, H. Ledbetter, J. B. Betts, Y. Zhao, L. L. Daemen, H. Cynn, and A. Migliori, Acta Materialia **57**, 544 (2009).

C. Pantea, I. Stroe, H. Lebetter, J. B. Betts, Y. Zhao, L. L. Daemen, H. Cynn, and A. Migliori, J. Phys. Chem. Solids **69**, 211 (2008).

T. G. Plymate and J. H. Stout, Phys. Chem. Min., **21**, 413 (1994).

V. B. Prakapenka, V. B., A. Kubo, A. Kuznetsov, A. Laskin, O. Shkurikhin, P. Dera, M. L. Rivers, and S. R. Sutton, H. Pres. Res., **28**, 225 (2008).

S. M. Rigden and I. Jackson, J. Geophys. Res., **96**, 9999 (1991)

K. Righter, Annu. Rev. Earth Planet Sci., **31**, 135 (2003)

M. Rivers, V. B. Prakapenka, A. Kubo, C. Pullins, C. M. Holl, and S. D. Jacobsen, High Pres. Res. **28**, 273 (2008).

B. Romanowicz, Annu. Rev Earth Plant. Sci. **31**, 303 (2003).

J. H. Rose, J. R. Smith, F. Guinea, and J. Ferrante, Phys. Rev B **29**, 2963 (1984)

W. L. Roth, Phys. Rev., 110, 1333 (1958).

J. P. Rueff, A. Mattila, J. Badro, G. Vankó and A. Shukla., J Phys.: Condens. Matt., **17**, S717 (2005).

Y. Sato, Equations of state of mantle minerals determined through high-pressure x-ray study. In: Manghnani M. H., Akimoto, S. (eds)High Pressure Research: applications in geophysics. Academic Press, New York, 307 (1977).

C. T. Seagle, D. L. Heinz, A. J. Campbell, V. B. Prakapenka, and S. T. Wanless, Earth Pl. Sci. Lett., **265**, 655 (2008).

J.F.A. Shackleford, CRC Handbook of Materials Science and Engineering; CRC Press: Boca Raton, FL, (2001).

C. G. Shull, W. A. Strauser, and E. O. Wollan, Phys. Rev., **83**, 333 (1951).

S. V. Sinogeikin and J. D. Bass, Geophys. Res. Lett., **28**, 4335 (2001)

G. Steinle-Neumann, L. Stixrude, R. E. Cohen, and O. Gülseren, Nature **413**, 57 (2001).

L. Stixrude and C. Lithgow-Bertelloni, Geophys. J. Int., **162**, 610 (2005).

Y. Sumino, M. Kumazawa, O. Nishizawa, and W. Pluschkell, J. Phys. Earth, **28**, 475 (1980).

I. Suzuki, E. Ohtani, and M. Kumazawa, J. Phys. Earth, **27**, 53 (1979).

B. Touzelin, Rev. Int. Hautes Temp. Réfr., **15**, 33 (1978).

J. Trampert, F. Deschamps, J. Resovsky, and D. Yuen, Science, **306**, 853 (2004).

G. A. Voronin, C. Pantea, T. W. Zerda, L. Wang, and Y. Zhao, J. Phys. Chem. Sol. **66**, 706 (2005).

U. D. Wdowik and D. Legut (2008), J. Phys. Chem. Sol., **69**, 1698 (2008)

M. B. Weinberger, J. B. Levine, H. Y. Levine, R. W. Cumberland, H. I. Rasool, J. M. Yang, R. B. Kaner, and S. H. Tolbert, Chem. Mater. **21**, 1915 (2009).

M. B. Weinberger, S. H. Tolbert, and A. Kavner, Phys. Rev. Lett. **100**, 045506 (2008).

D. R. Wilburn and W. A. Bassett, High Pres., **8**, 343 (1976)

C. S. Yoo, H. Cynn, P. Söderlind, and V. Iota, Phys. Rev. Lett., **84**, 4132 (2000).

C. S. Zha, W. A. Basset, and S. H. Shim, Rev. Sci. Instr. **75**, 2409 (2004).

V. N. Zharkov and V. A. Kalinin, Equations of state for solids at high pressures and temperatures, Consultants Bureau, New York (1971).

J. C. Zheng, Phys. Rev. B **72**, 052105 (2005).

A. Zerr, H. Reichmann, H. Euler, and R. Boehler, Phys. Chem. Min., **19**, 507 (1993).